

**In-situ vertical characteristics of optical properties and heating rates
of aerosol over Beijing**

Ping Tian¹, Dantong Liu^{2*}, Delong Zhao³, Chenjie Yu⁴, Quan Liu¹, Mengyu Huang¹, Zhaoze Deng⁵, Liang Ran⁵, Yunfei Wu⁶, Shuo Ding², Kang Hu², Gang Zhao⁷, Chunsheng Zhao⁷, Deping Ding^{1,3}

- 1. Beijing Key Laboratory of Cloud, Precipitation and Atmospheric Water Resources, Beijing, 100089, China.
- 2. Department of Atmospheric Science, School of Earth Sciences, Zhejiang University, Hangzhou, Zhejiang, 310027, China.
- 3. Field Experiment Base of Cloud and Precipitation Research in North China, China Meteorological Administration, Beijing, 100089, China.
- 4. Centre for Atmospheric Sciences, School of Earth and Environmental Sciences, University of Manchester, Manchester, M139PL, UK
- 5. Key Laboratory of Middle Atmosphere and Global Environment Observation, Institute of Atmospheric Physics, Chinese Academy of Sciences, Beijing, 100029, China.
- 6. CAS Key Laboratory of Regional Climate-Environment for Temperate East Asia, Institute of Atmospheric Physics, Chinese Academy of Sciences, Beijing, 100029, China.
- 7. Department of Atmospheric and Oceanic Sciences, Peking University, Beijing, 100871, China

Corresponds to: Dantong Liu (dantongliu@zju.edu.cn)

22 **Abstract.** Characterizing vertical profiles of aerosol optical properties is important because only relying
23 on the surface or column-integrated measurements is unable to unambiguously constrain the radiative
24 impacts of aerosol. This study presents series of vertical profiles of in-situ measured multi-wavelength
25 optical properties of aerosols during three pollution events from Nov. to Dec. 2016 over the Beijing region.
26 For all pollution events, the clean periods (CP) before pollution initialization showed a higher scattering
27 Ångström exponent and a smaller asymmetry parameter (g), and with relatively uniform vertical
28 structures. The heavy pollution (HP) periods showed increased particle size, causing these parameters to
29 vary in the opposite way. During the transition periods (TP), regional transport of aged aerosols at higher
30 altitude was found. The AERONET aerosol optical depth (AOD) matched the in-situ measurements
31 within 10 %, however the AERONET absorption optical depth (AAOD) was 10-20 % higher than the in-
32 situ measurements, and this positive discrepancy increased to 30 % at shorter wavelength. The absorption
33 of brown carbon (BrC) was identified by the increased absorption Angström exponent (AAE), and the
34 heating rate of black carbon (BC) and BrC was estimated by computing the spectral absorption coefficient
35 and actinic flux calculated by a radiative transfer model. BC and BrC had a heating rate up to 0.18 K/h
36 and 0.05 K/h in the planetary boundary layer (PBL) respectively during the pollution period. The fraction
37 of BrC absorption increased from 12 % to 40 % in the PBL from CP to HP period. Notably, a higher
38 contribution of BrC heating was found above the PBL under polluted condition. This study gives a full
39 picture of shortwave heating impacts of carbonaceous aerosols during different stages of pollution events,
40 and highlights the increased contribution of BrC absorption especially at higher altitude during pollution.
41

42 1 Introduction

43 The optical properties of aerosol, which is how aerosol scatters or absorbs solar radiation, have caused
44 important radiative impacts on earth system (IPCC2013). The optical properties depend on the particle
45 size (Bergin et al., 2001), refractive index (Ebert et al., 2002; Quinn, 2002) and mixing state of aerosols.
46 There are still large uncertainties in evaluating the radiative forcing of aerosol especially in east Asia
47 region due to lack of information on vertical distribution of these parameters (Liao and Seinfeld, 1998;
48 Ramanathan et al., 2001; Li et al., 2017). Previous studies showed that the surface observation or column-
49 integrated measurements may not provide sufficient information to derive vertical profiles of aerosol
50 optical properties (Andrews et al., 2011; Rosati et al., 2016). Modelling studies find the radiative forcing
51 impact is sensitive to the aerosol vertical distribution (Haywood et al., 1998), and especially for the
52 absorbing aerosol for example black carbon (BC) will exert different climatic impacts depending on the
53 location of the aerosol layer (Yu et al., 2002; Ban-Weiss et al., 2011; Wilcox et al., 2016). Though most
54 aerosols are contained inside the planet boundary layer (PBL), the climatic sensitivity to absorbing aerosol
55 rapidly increases with altitude (Ramanathan et al., 2001; Hodnebrog et al., 2014; Nazarenko et al., 2017).
56 Absorbing aerosol above the PBL has the potential to suppress the PBL development and enhance the
57 inversion cap at top of the PBL (Ding et al., 2016; Wang et al., 2018c), further aggravating the pollution.
58 However, this impact depends on the location of the absorbing layer which may also promote the
59 convection by heating the layer above (Koch and Del Genio, 2010; Yu et al., 2019). It is therefore
60 important to characterize the vertical profile of absorbing component in the atmosphere in order to
61 understand its influences on atmospheric thermodynamics.

62 The North China Plain (NCP) has raised great attention in the recent decade because of the severe air
63 pollution and high frequency of hazy days over this region. The causes of pollution have been widely
64 investigated through surface measurements (Zhang et al., 2013; Zhang et al., 2015; Zhong et al., 2018),
65 however only limited studies have considered the evolution of pollutants in the vertical direction (Tian et
66 al., 2019; Wang et al., 2018a). It was found that the surface aerosol concentration over Beijing not only
67 depended on the emission but also the vertical structure of the aerosol distribution, which was largely
68 dependent on local and synoptic meteorological conditions (Ran et al., 2016a; Zhao et al., 2019a), such

69 as the mountain chimney effect over the Beijing region which may introduce enhanced aerosol loading
70 to high altitudes (Chen et al., 2009). The light-absorbing aerosol mainly includes the species of black
71 carbon (Bond et al., 2013), brown carbon (Lack and Cappa, 2010) and dust (Klingmüller et al., 2019),
72 which have different spectral sensitivities to solar radiation. Different aerosol components dominate at
73 different environments, and the heating rates caused by various aerosol sources have been studied over
74 the world, e.g. for the anthropogenic sources over north America (Gao et al., 2008; Sahu et al., 2012; Liu
75 et al., 2015b), Europe (Ferrero et al., 2014; Ferrero et al., 2018) and south Asia (Chakrabarty et al., 2012;
76 Shamjad et al., 2015), and biomass burning sources over north and south America (Saleh et al., 2015;
77 Zhang et al., 2017). However, there is only sparse data regarding the vertical structures of heating rates.
78 The calculation were performed for single species such as BC or BrC but most did not consider the co-
79 impacts of all species (Chakrabarty et al., 2012; Chung et al., 2012; Shamjad et al., 2015). In the lower
80 free troposphere, the interaction of aerosol-induced heating with boundary layer dynamics has raised
81 much attention recently, as it may play important role in suppressing boundary layer development hereby
82 exacerbating the local pollution (Li et al., 2017). The heating rate caused by light absorbing aerosol was
83 reported to vary as a function of height and range at 0.3-2.1 K/day for the polluted PBL over Europe
84 (Kedia et al., 2010; Ferrero et al., 2014; Ferrero et al., 2018), and 0.3-2.5 K/day for south Asia (Tripathi
85 et al., 2007; Ramana et al., 2007; Ramachandran and Kedia, 2010; Chakrabarty et al., 2012). Only a
86 limited number of reports are available for east Asia.

87 This study chose three typical pollution events occurring in wintertime over Beijing, and performed
88 continuous flights on daily basis for each event. The vertical profiles of multi-wavelength aerosol optical
89 properties were in-situ characterized, accounting for all stages during pollution events from the pollution
90 start, full development and cease. The directly measured optical parameters were used as inputs for
91 radiative transfer calculation, hereby the heating rates of light-absorbing aerosols, including black and
92 brown carbon (BrC) were estimated. The results here provide a full picture of vertical profiles of aerosol
93 optical properties over Beijing region and investigate the radiative forcing effect of aerosol during the
94 heavy pollution events.

95 **2 Instrumentation and data analysis**

96 A Kingair 350ER turbo aircraft in Beijing weather modification office was employed for the in-situ
97 measurements over Beijing during the 2016 winter in this study. Meteorological parameters including the
98 temperature, relative humidity, pressure, wind direction and wind speed with a time resolution of 1 s were
99 measured by the Aircraft Integrated Meteorological Measurement System (AIMMS-20, Aventech
100 Research Inc, Canada), which was calibrated annually. The aerosol instrumentation inside the cabin was
101 connected to an isokinetic inlet (Model:1200, Brechtel Inc, USA), which can deliver particle with a high
102 transport efficiency (90%) for sub-micrometer particles. The room temperature (25 °C) in the cabin had
103 a self-drying effect when the temperature inside was higher than outside the cabin, in addition to which,
104 a silicate dryer was used of all instruments to maintain a sampling RH lower than 40%.

105 In-situ measurements of aerosol optical properties were performed during three pollution events over
106 Beijing in Nov. 15th to Dec. 21th 2016, including 14 flights covering the start, development and cease
107 stage for each pollution event. All flights were conducted around midday when the PBL was well
108 developed. Table 1 summarizes the information of each flight. In order to compare the AOD from
109 AERONET and to calculate the vertical heating rates, only the cloud-free vertical profiles are used. In
110 this study, three flights (20161117 12:00, 20161117 15:00, 20161118 12:00) were observed with cumulus
111 clouds (Table 1). The in-cloud data in this study was screened out according to the in-situ measured cloud
112 number concentration and liquid water content. Data with a total number concentration of more than 10
113 cm⁻³ and liquid water of more than 0.001 g m⁻³ are not included in the following analysis (Deng et al.,
114 2009). A micro pulse lidar (MPL, Sigma Inc, USA) was employed to measure the temporal evolution of
115 aerosol extinction vertical profiles, and the vertical wind profile was measured by a wind profile radar
116 with a vertical resolution of 150 m.

117

118 2.1 Aerosol optical properties

119 The aerosol scattering (σ_{sca}) and hemispheric backscattering (σ_{bsca}) coefficients at $\lambda=450$ nm, 525 nm, and
120 650 nm were measured by an integrating nephelometer (Aurora3000, Ecotech Inc, Australia), and the
121 flowrate of Aurora3000 was maintained at 4 L/min during flight. The baseline of Aurora3000 in real time

was corrected for Rayleigh scattering of gas molecule at different air pressure (Fig. S1). In addition, the σ_{sca} and σ_{bsca} at all wavelengths were corrected for truncation affects (Anderson and Ogren, 1998; Müller et al., 2009).

The scattering Ångström exponent (SAE) measures the wavelength dependence of σ_{sca} assuming a power relationship with λ , expressed as:

$$SAE = -\frac{\ln(\sigma_{\lambda_1}/\sigma_{\lambda_2})}{\ln(\lambda_1/\lambda_2)}, \quad (1)$$

where σ_{λ_1} denotes the σ_{sca} at λ_1 , the value of SAE could also be used to reflect particles size with larger particles showing a smaller SAE (Carrico et al., 1998).

The asymmetry parameter (g) is obtained from measured backscattering fraction according to the empirical function from Andrews et al. (2006).

$$g = -7.143889 \cdot \beta^3 + 7.4633439 \cdot \beta^2 - 3.9356 \cdot \beta + 0.9893, \quad (2)$$

where β is the hemi-spherical backscatter fraction ($\sigma_{bsca}/\sigma_{sca}$) measured by the Aurora3000.

The absorbing coefficient (σ_{abs}) at different wavelengths (370, 470, 520, 590, 660, 880, and 950nm) was measured by an Aethalometer (AE33, Magee Scientific Inc, USA) (Hansen, 2005). The flowrate of AE33 was maintained at 4 L/min below 3000 m. The shadowing effect of the AE33 was corrected by the two spot measurements with different attenuation (Drinovec et al., 2017). The multiple scattering artifact of the AE33 was corrected by measuring the ambient aerosol in parallel with a photoacoustic spectrometer (PASS3, DMT Inc, USA), and the latter is independent of the filter artifacts. The PASS3 was calibrated using the NO₂ and BC standard (Arnott et al., 2005). Fig. S2 shows the two weeks' ambient measurements between AE33 and PASS3 at three overlapped wavelengths. Multiple-scattering correction factor of 2.88 was consistently found at three λ , which was applied to correct the AE33 measurement.

The absorbing Ångström exponent (AAE), which can weight the absorption at different wavelengths, is calculated using power fitting function at seven wavelengths.

$$\sigma_{abs}(\lambda) = \sigma_{abs,0} (\lambda/\lambda_0)^{AAE}, \quad (3)$$

We estimated σ_{abs} of BrC assuming that BC is the only absorber at $\lambda=950$ nm, then the absorption of BC

at other wavelengths was extrapolated by assuming an AAE of 1 (Kirchstetter et al., 2004; Lack et al., 2013; Massabò et al., 2015), and the contribution of BrC at each wavelength was obtained by subtracting the BC absorption from the total absorption (Schnaiter et al., 2005; Liu et al., 2015a). It should be noted that previous studies pointed out the AAE_{BC} may be less than 1, thus assuming $AAE_{BC}=1$ may lead to an underestimation of BrC contribution (Gyawali et al., 2009; Lack and Cappa, 2010; Feng et al., 2013). We therefore consider the results reported here is the lower bound for the BrC contribution.

The single scattering albedo (SSA) is the ratio of the scattering coefficient over the extinction coefficient (σ_{ext}) at a given wavelength.

The parameters σ_{sca} , σ_{abs} , and σ_{ext} are reported for standard temperature and pressure (STP, 1013.25 hPa, 273.15K) to allow for direct comparison at different altitudes among flights. Note that to compare with the AERONET results and for the radiative transfer calculations (as detailed in the following), these parameters in ambient conditions are used.

Column aerosol optical properties during the aircraft observation period were obtained from the Aerosol Robotic Network (AERONET) sun-photometer network (Che et al., 2009; Xia et al., 2008), where the site (AERONET BEIJING_PKU) is about 10 km away from the location of the vertical profiles. The measurement of σ_{ext} was up to 2500m above which the aerosol concentration was low enough to be below the instrument lower detection limit. Given the very low concentration above 2500m, the value at 2500m was used to reconstruct the vertical profile up to 5000m. After that the σ_{ext} from 2.5-5 km only accounted for 1-2 % of the integrated columnar extinction.

To evaluate the potential influence of the particle hygroscopicity on optical properties, the aerosol hygroscopic growth parameterization ($f(RH)$) is used to calculate the enhancement of σ_{sca} under ambient RH. This function was previously measured by Zhao et al. (2019b) over Beijing region, expressed as:

$$f(RH) = a \cdot (1 - RH/100)^{-\gamma(RH/100)} \quad (4)$$

where $f(RH)$ was obtained by a comparison between a dry and humidified nephelometers in parallel. a / γ was 0.930 / 0.329, 0.971 / 0.372, and 0.988 / 0.356 for clean, moderate, and heavy pollution period, respectively, according to the study.

173 The RH influence on g was calculated according to Zhao et al. (2018), expressed as:

174
$$g(RH)/g(RH < 40\%) = a \cdot (1 - RH/100)^{-\gamma(RH/100)} \quad (5)$$

175 where a / γ was 0.9984 and 0.0849.

176 The σ_{sca} , σ_{ext} , SSA , and g are all calculated for the hygroscopicity influence.

177

178 2.2 Radiative transfer calculation

179 The atmospheric irradiance and actinic flux using the pseudo-spherical version of the Discrete Ordinates
180 Radiative Transfer Code (DISORT), as implemented in the libRadtran software package (Emde et al.,
181 2016). The in-situ measured vertical profiles of AOD, single scattering albedo (SSA), and g are used as
182 inputs, and the other input parameters for the radiative transfer calculation are summarized in Table 2.
183 The calculation is performed for clear-sky condition only, thus the flights experiencing low-level clouds
184 are not included in the calculation. The direct, upward diffuse, and downward diffuse irradiance and
185 actinic flux (AF, in mWm^{-2}) at $\lambda = 250\text{-}2550$ nm are calculated. The calculation of AF is performed with
186 and without the aerosol input (AOD is set to zero) to evaluate the aerosol net impact. The heating rate is
187 only calculated with considering the in-situ measured AOD. The spectral instantaneous absorbing power
188 of BC (A_{BC}) or BrC (A_{BrC}) can be calculated by multiplying the absorption coefficient of BC (or BrC) and
189 AF at specified λ , then integrating all λ will obtain the total absorbing power (Gao et al., 2008; Emde et
190 al., 2016), expressed as:

191
$$A_{BC \text{ or } BrC} = \int_{250\text{nm}}^{2550\text{nm}} AF(\lambda) \cdot \sigma_{BC \text{ or } BrC}(\lambda) d\lambda, \quad (6)$$

192 By assuming no radiative loss of solar energy and that the heat absorbed by aerosol is fully transferred to
193 the surrounding air, the instantaneous heating rate of BC or BrC to the ambient air is hence calculated as:

194
$$H_{BC, BrC} = A_{BC, BrC} / (\rho \cdot C_p), \quad (7)$$

195 where ρ and C_p are the air mass density (kg/m^3) and heat capacity ($1.007 \text{ J/g}\cdot\text{K}$), respectively. The profiles
196 of aerosol optical properties influenced by hygroscopic growth (as calculated above) are also input in the

197 calculation to work out its influence on heating rates.

198

199 3 Results and discussions

200 3.1 Overview and the pollution events

201 Three pollution events from Nov. 15th to 18th (Case 1), Dec. 10th to 12th (Case2), and Dec. 16th to 19th
202 (Case 3) in 2016 were captured. Figure 1 shows the temporal evolution of surface PM_{2.5}, AOD (AAOD)
203 constrained by the in-situ aircraft measurements and from the AERONET, and the vertical profiles of σ_{ext}
204 and wind information during the Case 1 pollution event. The other two events are shown in Fig. S3 and
205 Fig. S4. Aircraft vertical profiles were performed on a daily basis as the flight time being indicated by the
206 vertical bars (Fig. 1). Each pollution event was classified as pollution initialization, development and peak
207 pollution period, corresponding to the pollution levels as clean period (CP, PM_{2.5, surface} < 35 $\mu\text{g}/\text{cm}^3$),
208 transition period (TP, 35 $\mu\text{g}/\text{cm}^3$ < PM_{2.5, surface} < 200 $\mu\text{g}/\text{cm}^3$) and heavy pollution (HP, PM_{2.5, surface} > 200
209 $\mu\text{g}/\text{cm}^3$). Three flights (20161117 12:00, 20161117 15:00, 20161118 12:00) experienced boundary layer
210 cloud (Fig. 1c), as indicated by the intensive extinction on top of the PBL. There were 3, 4 and 4 profiles
211 in clear sky condition for the CP, TP and HP period respectively (as detailed in Table 1). As Fig. 1b shows,
212 wind sheers in both wind speed and direction appeared on top of the PBL, consistent with the vertical
213 distribution of σ_{ext} observed by a lidar (Fig. 1c). During the CP, wind profiles (Fig. 1b) showed dominant
214 northwesterly wind with high wind speed throughout the column, dispersing the pollutant in a more
215 developed PBL (Fig. 1c). During the TP, the southerly air flow dominated and the PM_{2.5} mass
216 concentration underwent a rapid increase from 30 to 100 $\mu\text{g m}^{-3}$ in several hours. During HP, the
217 windspeed was relatively low at all altitudes, maintaining the PM_{2.5} mass concentration at a high level.

218 Figure 2 summarized the in-situ measured meteorological parameters at different stages of pollution
219 events. The height of PBL (PBLH) was determined by considering a variety of factors. Firstly, a stable
220 potential temperature (θ) (Fig. 2d-f) with vertical gradient $d\theta/dz < 5$ K/km in the PBL indicated an
221 sufficient convective mixing (Su et al., 2017), with a pronounced positive gradient above the PBL
222 indicating a stable layer (Petra Seibert, 2000). Secondly, there was usually a temperature inversion on top

of the PBL (Fig. 2a-c). During the CP, the weak temperature inversion ($\sim 0.15\text{K}/100\text{m}$) on top of the PBL allowed pollutants to penetrate the PBL and disperse in a higher atmospheric column (Fig. 2b). This inversion was significantly enhanced for the TP and HP periods, to $0.9\text{K}/100\text{m}$ and $0.7\text{K}/100\text{m}$ respectively. The large increase of the inversion during flight 20161211 was caused by the regional transport from the south, when the lower-latitude warmer air mass was imposed onto the measurement level (Tian et al., 2019). Additionally, the PBLH decreased gradually as the pollution continued during the pollution event, in line with the enhanced aerosol concentration in the PBL. The moisture had similar features that a lower moisture content showed when lower pollution level and was vertically efficiently dispersed; whereas the stronger inversion trapped the moisture inside the PBL, leading to a positive vertical gradient with the maximum RH showing on top of the PBL. There were some regional transport influences under TP, resulting in enhanced RH when air mass was advected from the south (Fig. 2f).

234

235 3.2 Vertical profiles of σ_{ext} , σ_{sca} and σ_{abs}

Figure 3 shows the vertical distributions of aerosol optical properties including extinction (σ_{ext}), scattering (σ_{sca}) and absorbing (σ_{abs}) coefficients. Different structures of vertical profiles were observed for CP, TP and HP periods. During the CP, aerosol concentration was low and showed a uniform mixing inside the PBL, with the σ_{ext} , σ_{sca} and σ_{abs} ranging from $220\text{-}270\text{ Mm}^{-1}$, $180\text{-}240\text{ Mm}^{-1}$, and $30\text{-}50\text{ Mm}^{-1}$, respectively. The backward trajectories for the CP showed that the air masses were from the northwestern low emission region (Fig. S5). TP showed about a 4-fold increase of σ_{ext} compared to the CP. During the TP, the σ_{ext} , σ_{sca} and σ_{abs} had large variation inside the PBL, ranging from $325\text{-}1435\text{ Mm}^{-1}$, $300\text{-}1275\text{ Mm}^{-1}$, and $45\text{-}160\text{ Mm}^{-1}$, respectively, and the mean PBLH decreased to $200\text{-}500\text{ m}$. During these pollution accumulation periods (before the pollution reached the peak level), two contrast vertical structures was observed. One showed a well-mixing in the PBL but declined concentration in the free troposphere (FT) (e.g. flight 20161115PM and 20161210) (Fig. 3a). The other one had the increased aerosol layer on top of the PBL, and showed positive vertical gradients for all optical properties at a certain level (e.g. flight 20161116 AM, 20161211 and 20161216) (Fig. 3b). The former was because of the mostly cleaner northwesterly air mass and higher wind speed influencing the layer above the PBL, while the latter

250 resulted from the southwesterly regional transport (Tian et al., 2019).

251 During the HP period, most flights consistently showed the exponentially-declined vertical profile
252 patterns, and the PBLH was even lower than that during the TP (Fig. 2f). The stronger temperature
253 inversion (Fig. 2c) and lower wind speed (Fig. 1b) inside the PBL led to high stability of the PBL and
254 promoted the pollutant accumulation. The aerosol concentration was largely enhanced towards the surface
255 and sharply declined above the PBL. Interestingly, the absorption showed a higher degree of negative
256 vertical gradient than the scattering at $\lambda=440\text{nm}$, which may reflect the different sources and mixing ratios
257 of absorbing and non-absorbing aerosols. The surface emission tends to contain more primary sources of
258 absorbing particles such as BC and BrC, while enhanced secondary aerosol formation at upper altitudes
259 may add additional aerosol extinction.

260 The vertical profiles of σ_{sca} and σ_{abs} during HP can be fitted as:

261
$$\sigma_{sca} = \sigma_{sca,0} \cdot \exp(-a * H); \quad a = 0.0012 \pm 0.0001, \quad (8)$$

262
$$\sigma_{abs} = \sigma_{abs,0} \cdot \exp(-b * H); \quad b = 0.0015 \pm 0.0001, \quad (9)$$

263 where σ_0 represents the surface value of σ_{sca} and σ_{abs} , and H is the altitude. The a and b are the parameters
264 defining the changing rate with altitude. This parameterization could be used to represent the vertical
265 structure of optical properties under heavy pollution condition.

266 The hygroscopic effect on aerosol vertical profiles was mainly controlled by the ambient RH (shown in
267 blue lines in Fig. 3). For most of the flights, the hygroscopic effect could be neglected due to low RH (<
268 50%) (Fig. 2). For some of the flights (20161211), the σ_{sca} and σ_{ext} especially at top of the PBL could be
269 enhanced by a factor of 1.3.

270

271 3.3 Vertical profiles of SSA, SAE, AAE and g

272 Figure 4 shows the vertical profiles of SSA, SAE, AAE, and g for all the flights during different stages of
273 pollution events. Overall, the SSA showed two modes inside the PBL. During the CP, SSA for most flights
274 was populated at 0.85, and had less variation throughout the column in the PBL. Flight 20161115AM

showed a strong elevation of *SSA* (0.94) at 2200 m (Fig. 4a), which may be influenced by a dust layer (to be further discussed below). *SSA* showed a positive vertical gradient for the TP and HP inside the PBL, i.e. from the surface to the PBLH, the mean *SSA* increased from 0.85 to 0.91 and from 0.87 to 0.92 for the TP and HP period, respectively. This indicates the reduced fraction of absorbing particles, in turn suggesting an enhancement of secondary production for non-absorbing particles. There were a few profiles featuring with a large enhancement of *SSA* (>0.95, for flight 20161211) at high altitude (Fig. 4b), and backward trajectory analysis (Fig. S5) showed that these resulted from the regional transport when more aged pollutants were advected to the high altitude. The *SSA* in the FT was mostly higher than that in the PBL and maintained at 0.9-0.95 for the TP and HP, suggesting a lower absorbing particle fraction at higher altitudes. Comparing among different stages during pollution events, it could be concluded that at the initialization stage of the pollution when the total PM was relatively low, a lower *SSA* exhibited, while the increase of pollution level added more secondary substances, hence increasing *SSA*. This trend was consistent with the previous ground studies in Beijing (He et al., 2009; Jing et al., 2011).

The *SAE* reflects the particle size with larger size having a smaller *SAE*. A decreasing *SAE* was shown for increasing pollution levels inside the PBL (Fig. 4), i.e., from the CP to HP, the *SAE* in the PBL showed an average value of 1.74, 1.45, and 1.21, respectively. For most of the profiles, *SAE* showed enhancement at higher altitudes. This means smaller particle sizes were present at higher altitudes, which may result from a higher scavenging efficiency for larger particles whereas smaller particles remained un-scavenged at the upper height (Liu et al., 2009). These was an exception for flight 20161211, when the regional advection transported larger and aged particles to the higher altitude. The particle size also corresponded with the asymmetry parameter (*g*, Fig. 4j-i), with larger particle representing more fraction of forward scattering (larger *g*). Note that there was only one flight (flight 20161211) under RH > 80 %, where the particle hygroscopicity had appreciable influences on *SSA* (increased by 0.05), *SAE* (decreased by 0.2) and *g* (increased by 0.1).

AAE reflects the degree of the absorption towards shorter wavelength, such as the presence of BrC will enhance the absorption in the UV. A lower *AAE* of 1.2 ± 0.2 was shown for the CP (Fig. 4g), but it increased to 1.56 ± 0.3 for TP in the PBL (Fig. 4h), and an additional higher mode of *AAE* showed at 1.8-2.0 for the HP period (Fig. 4i). There was a weak variation of *AAE* for CP throughout the column, but

became largely spread for TP, i.e., with either positive or negative vertical gradient at different altitudes. Notably, the *AAE* showed consistent positive vertical gradient for most of the HP profiles (Fig. 4i). This implied the enhancement of BrC contribution at higher altitude for the polluted troposphere. Flight 20161115AM showed a notably increased *AAE* up to 2 at altitude 2 km (Fig. 4g), which may reflect the influence of dust (Cazorla et al., 2013). The ground *AAE* had strong seasonal variation with winter normally showing a higher *AAE* due to higher emissions of solid fuel burning (Sun et al., 2017; Wang et al., 2018b). However, there is still lack of results on the vertical characteristics of *AAE* due to limited measurements, and the results here highlight the enhancement of BrC at higher level, mainly for polluted environment.

312

3.4 Comparison of column integrated and in-situ constrained AOD/AAOD

To compare the AOD and AAOD between the AERONET and that constrained by the in-situ measurements, the AERONET data was chosen to match with the aircraft profiles in time (± 3 h) and location (within 10 km) (the PEK site). The comparison was performed at overlapped wavelengths (440nm, 675nm, and 870nm) between AERONET and aircraft instruments. As Fig. 5a-c shows, high correlation ($R^2 > 0.95$) was found between the columnar and in-situ measurements. In particular, the correlation was close to unity for dry conditions ($RH < 40\%$), while the AERONET data was about 10-20% higher than the in-situ measurement for $RH > 60\%$. Improved agreement was achieved by 8-15% if considering aerosol hygroscopic growth (open circle in Fig. 5a-c), despite that the in-situ constrained AOD was still 2-5% lower than the AERONET after the hygroscopic correction.

Figure 5g-i shows at three wavelengths the AAOD had lower correlations between both methods compared to AOD, with $R^2 = 0.75, 0.58, \text{ and } 0.49$ at 440 nm, 675 nm, and 870nm, respectively. The columnar AAOD was overall about 10-25% higher than the in-situ measurement, and this AERONET AAOD overestimation was higher under higher AOD conditions. This is consistent with previous findings conducted over the USA that the AAOD retrieved from AERONET was biased higher when compared to the in-situ measurement (Andrews et al., 2017).

Note that there was better **agreements** during the CP, when lower pollution level and lower RH (shown in blue dots). This suggests a lower moisture and less AOD **interference** may improve the agreement **on** AAOD. **Previous** studies pointed out that the retrieval **from** the AERONET was sensitive to the variation of aerosol vertical distribution (Torres et al., 2014). We **thus** speculate that the better agreement for CP was due to the vertically homogeneous distribution of aerosol optical properties, and **the** larger bias for **the** TP and HP periods might be caused by the significant variations of the vertical profiles. Other factors like the aerosol hygroscopic growth under higher RH may introduce factors in enhancing the absorption, e.g. more lensing **effects** on BC absorption via thicker and moisture **coatings** (Wu et al., 2017). Though this study is not able to rule out the exact influencing factor in causing this discrepancy, an overestimation of 25% in the AERONET AAOD under polluted **conditions** is shown for the dataset here.

3.5 Heating impacts of BC and BrC

Figure 6 shows vertical profiles of irradiances from **the** radiative transfer calculation using in-situ measurements as model inputs (Table 1). The results show that the presence of aerosols reduced the direct irradiance reaching the surface (Fig. 6a-c) but increased the upward diffuse (Fig. 6d-f) and downward diffuse irradiances, especially above the PBL (Fig. 6g-i). The direct irradiance on the surface ranged from 1×10^9 to 3.5×10^9 mW m⁻², with an average of 2.2×10^9 mW m⁻² during **the** CP (Fig. 6a), which was about two-fold and three-fold larger than that during **the** TP (Fig. 6b) and HP period (Fig. 6c), respectively. The combined direct, diffuse upward and downward **irradiances** which forms the actinic flux (AF), showed an enhancement above the PBL and a reduction within the PBL (Fig. 7a-c), but to what extent the enhancement or reduction occurred **depended** on the aerosol vertical **profiles**. The vertical gradient of AF was slightly modified by **the** aerosol loadings during **the** CP, whereas for the TP and HP, aerosol effects caused AF about two times smaller within the PBL and 20 % larger above the PBL, leading to an increased vertical gradient of AF. The AF received at lower **altitude** was reduced by up to 10 % by incorporating the aerosol hygroscopicity influence (Fig. 7) due to **the** enhanced AOD, and AF was further redistributed to give **a** larger vertical gradient (Fig. 7a-c).

The vertical profiles of absorbing power and heating rate of BC are shown in Fig. 7d-f. Vertically homogeneous BC heating **rate** of 0.05 K/h was found inside the PBL during **the** CP (Fig. 7d). During the

356 regional transport cases (flight20161211 and flight20161216) for the TP, positive vertical gradients
357 (increase with increasing altitude) of BC heating rates were observed, and as high as 0.1 K/h heating rate
358 could occur at top of the PBL (Fig. 7e). During the HP period, negative heating rate (decrease with
359 increasing altitude) of BC was found except for one flight on 20161212 in Case 2, and the BC heating
360 rate at the surface could reach as high as 0.15 K/h (Fig. 7f). The reason causing the negative vertical
361 gradient of BC heating rate was the higher degree of negative gradient of σ_{abs} (Fig. 3i) than the positive
362 gradient of AF (Fig. 7). The results here show that the atmospheric heating by aerosol was mainly inside
363 the PBL and for polluted period the BC-induced heating was 0.05-0.17 K/h, generally consistent with
364 previous studies over the polluted Asia region, with 0.02-0.17 K/h (Ramana et al., 2007; Ramana et al.,
365 2010; Kedia et al., 2010).

366 The contribution of BrC to absorbing power and heating rate was computed as the integrated portion of
367 absorption over the visible wavelength (370–950nm in this study) by subtracting the BC absorption from
368 the spectrum. Figure 7g-i shows the vertical profiles of BrC heating rate. Continuously increase of BrC
369 heating rate in the PBL was observed from CP to HP, with mean heating rate of 0.02 K/h, 0.03 K/h, and
370 0.05 K/h during the CP, TP and HP respectively. Though the BC was the main contributor to the heating
371 in the PBL, the heating of BrC was more evenly distributed and could be comparable with the BC heating
372 rate at high altitude especially during the HP period (Fig. 7i). The contribution of BrC to the total
373 absorption was reported to be 10-27 % over the polluted region of Europe (Ferrero et al., 2018) and south
374 Asia (Chung et al., 2012; Shamjad et al., 2015), in general consistent with the results during polluted
375 periods here.

376 Corresponding with the aerosol hygroscopicity influence on the actinic flux, the heating rate showed
377 lowered intensity but enhanced vertical gradient for the flights with high ambient RH (Fig. 7b). The
378 vertical gradient of the overall heating rate from absorbing components, i.e. increase or decrease heating
379 rate with altitude, will importantly determine the influence on atmospheric stability. If the heating
380 occurred near surface (Case 3), the lower layer will be heated leading to an enhanced convective mixing
381 (Sühring et al., 2014; Petaja et al., 2016); whereas if the heating was above the PBL (Case 2), an increase
382 of temperature inversion will occur hence inhibiting the PBL development and trapping the pollutants in
383 the PBL (Chakrabarty et al., 2012; Tripathi et al., 2007). This study showed positive vertical gradients for

384 30 % of the flights especially during the regional transport when pollutants were advected from outside
385 of Beijing and showed elevation of absorption at higher altitude (Fig. 8). The rest of the flights showed
386 highly accumulated aerosol concentration near surface, and BC potentially promoted the dispersion in the
387 PBL and decreased its stability. This was also found by a previous study (Ferrero et al., 2014).

388 3.6 The importance of BrC heating effects

389 Figure 8 shows the measured absorption coefficient of BrC and BC inside and above the PBL at different
390 λ for CP, TP and HP period, respectively. The results suggested that both σ_{abs} of BC and BrC increased
391 with the pollution level, e.g. the σ_{abs} at $\lambda=440\text{nm}$ was 42.8 Mm^{-1} and 7.2 Mm^{-1} on average in the PBL
392 and above the PBL respectively during the HP, and was 4.7 Mm^{-1} and 1.3 Mm^{-1} for the CP. The
393 contribution of BrC to total σ_{abs} was found to increase from the CP to the HP period (Fig. 8c, f). This is
394 in line with previous studies in urban Beijing that more BrC contribution to total absorption was found
395 under higher pollution level (Ran et al., 2016b; Xie et al., 2019), suggesting the important role of BrC on
396 absorption under polluted condition.

397 The contribution of BrC to total heating rates showed notably different vertical structures. During the CP,
398 all profiles showed consistently low BrC contribution throughout the column, with about 7 % at the
399 surface and 9 % in the FT (Fig. 8g). This means the low primary emission or the emission after being
400 diluted by clean air mass did not contained a large fraction of absorbing organics. During the TP, BrC
401 contribution inside the PBL increased to 22 % and showed considerable variations at higher altitude (Fig.
402 8h). During the HP period, the surface contribution was comparable with that in TP, but showed
403 remarkably enhanced BrC heating contribution at higher altitudes, with a vertically increasing rate of
404 $1.5\text{ \%}/\text{m}$ in the PBL and reached as high as 45 % in the LFT. The higher heating contribution of BrC at
405 higher altitudes means the BrC absorption played an important role in heating at upper altitudes, which
406 may enhance the temperature inversion at that level hereby inhibiting the convective mixing under the
407 heated layer.

408 By comparing the BrC heating contribution at the surface, there was an increase from CP to TP, however,
409 not from TP to HP. This suggests the primary emission will increase the BrC fraction from CP to TP, but

for even more polluted environment from TP to HP, the primary emission may provide limited further increased fraction of BrC. The primary BrC could result from a range of combustion sources, and the polluted region at the south of Beijing contained a higher fraction of residential coal burning sources (Sun et al., 2017; Xie et al., 2019) which may influence the Beijing region under polluted period in wintertime. The relatively consistent BrC contribution at ~20 % from TP to HP suggested the relatively uniform BrC profiles for the primary sources. During the TP, the BrC contribution above the PBL had rarely been above 30 % (Fig. 8h), however during the HP, there was a further enhancement of BrC contribution up to 45 % above the PBL (Fig. 8i). Note that there was no direct injection of biomass burning plume to the high altitude during the study period, the higher portion of BrC absorption above the PBL during HP may be formed through secondary production in addition to the primary source contribution. As Fig. 7a-c shows, there was more intensive actinic flux received at higher altitude and this may promote the photochemical reactions of gas-phase species, allowing more secondary formation of aerosol which may contain a fraction of BrC (Feng et al., 2013; Nakayama et al., 2013). Previous studies also found enhanced BrC formation with light source under certain RH (Nguyen et al., 2012; Updyke et al., 2012; Laskin et al., 2015; Zhao et al., 2015). The positive gradient of BrC heating contribution was more likely resulted from the enhanced RH from the surface to the top of PBL (Fig. 2i), because increased moisture will promote the aqueous reaction and gas-to-aerosol partition which may also form part of the BrC observed here (Ervens et al., 2011; Nakayama et al., 2013). The secondary formation of BrC also requires the inorganic or VOC precursors being transported to the high altitudes, therefore the enhancement of BrC mostly occurred under higher pollution level when sufficient gas precursors were transported to higher altitudes. The BrC may be also subject to bleaching process and lose the absorbance (Sareen et al., 2013; Lee et al., 2014; Wong et al., 2019), because the profiles in this study were conducted over an urban megacity where the sampled pollutants were fairly young and may have not experienced sufficient ageing for BrC to be degraded.

4 Conclusions

This study provides detailed characterization of vertical profiles of aerosol optical properties over the Beijing region by continuous aircraft in-situ measurements at different stages during the pollution events.

437 The results combining direct measurements of scattering and absorption at multiple **wavelengths**, give a
 438 full picture of how the optical properties had evolved at different layers during typical pollution **events**.
 439 During **the** clean period for pollution initialization (CP), the aerosols showed relatively uniform
 440 characteristics throughout the planetary boundary layer (PBL) and lower free troposphere (FT), such as **a**
 441 lowing scattering or absorption coefficient, larger *SAE* (due to smaller particle size) and lower fraction of
 442 brown carbon (BrC), **as reflected by a smaller *AAE***. The transition period (TP) when pollution was
 443 developing had large **variations** of all optical properties, and enhanced aerosol loadings at higher altitude
 444 were encountered when being influenced by regional advection. The fully developed heavy pollution
 445 period (HP) featured with the shallow PBL accumulated over 80 % of the scattering and absorption within
 446 the PBL, and deceased *SAE* due to **the** enlarged particles size. Notably the absorption towards shorter
 447 wavelength became larger under more polluted environment, especially **at** the higher altitude.

448 The AOD and AAOD measured by **the** passive remote sensing was for the first time compared with in-
 449 situ measurements over this polluted region. AOD showed high correlation between **the** AERONET and
 450 in-situ measurement within 10 %, and the most discrepancy between both could be possibly resolved by
 451 considering the hygroscopic growth of aerosols under high RH condition. The AAOD however showed
 452 10-25 % higher for **the** remote sensing especially at shorter wavelength, consistent with other studies
 453 (Müller et al., 2012; Andrews et al., 2017). The possibilities of causing this could be the non-
 454 homogeneously vertically **structures** of optical properties, mixing state of light-absorbing aerosol, and
 455 also the particle hygroscopic growth, which are unable to be **elucidated** only using the results here.

456 BC was the main heating species, **inducing** 0.05 K/h, 0.1 K/h and 0.15 K/h heating rate at local **times**
 457 **from** 12:00 to 15:00 in the PBL during pollution initialization, transition and full development,
 458 respectively. **The heating rate** showed positive vertical gradient during **the** regional transport period when
 459 pollution was advected **to a high altitude** from the polluted **southern region** of Beijing (Tian et al., 2019).
 460 The contribution of BrC to **the** heating rate was found to increase by 20 % throughout the column from
 461 **the** CP to **the** HP period, in particular the increased BrC contribution was pronounced at the layer above
 462 the PBL during **the** HP, which was proposed to result from intensive photochemical reactions above the
 463 PBL. The BrC present at this layer will have the potential to contribute to the heating, hence enhancing
 464 the temperature inversion on top of the PBL hereby **its** the capping effect to the pollutants. Particles at

465 higher altitude may be transported to wider **regions** spatially in both vertical and horizontal directions,
466 which may lead **the** BrC present at this layer to have wilder and longer radiative impacts. Different
467 **mechanisms** of BrC formation at different levels such as above the PBL (where more solar flux received)
468 or within the PBL (where more moisture was constrained) warrants future **study**.

469

470

471 **Data availability.** All data in this paper are available from the authors upon request
472 (tianping@bj.cma.gov.cn).

473 **Competing interests.** The authors declare no conflicts of interest.

474 **Author contribution.** D. D., and M. H., led and designed the study; P. T., and D. L., designed the study,
475 set up the experiment, analyzed the data, and wrote the paper. P. T., D. Z., and Q. L., conducted the aircraft
476 observation. C. Y., performed the radiative transfer model calculation. P. T., D. L., Z. D., L. R., and Y. W.,
477 contributed to the aircraft data analysis. S. D., and K. H., contribute to the surface data analysis. G. Z.,
478 and C. Z., conducted the aerosol absorption comparison experiment.

479 **Acknowledgment.** This research was supported by the National key Research and Development Program
480 of China (2016YFA0602001), the National Natural Science Foundation of China (41875044, 41875167,
481 41675038, 41975177), and the Beijing Natural Science Foundation (8192021). Part of this work is
482 supported by the National Center of Meteorology, Abu Dhabi, UAE under the UAE Research Program
483 for Rain Enhancement Science.

484

485 **Reference**

- 486 Anderson, T. L., and Ogren, J. A.: Determining Aerosol Radiative Properties Using the TSI 3563
 487 Integrating Nephelometer, *Aerosol Sci. Technol.*, 29, 57-69, 10.1080/02786829808965551, 1998.
- 488 Andrews, E., Sheridan, P. J., Fiebig, M., McComiskey, A., Ogren, J. A., Arnott, P., Covert, D., Elleman,
 489 R., Gasparini, R., Collins, D., Jonsson, H., Schmid, B., and Wang, J.: Comparison of methods for deriving
 490 aerosol asymmetry parameter, *J. Geophys. Res.*, 111, 10.1029/2004jd005734, 2006.
- 491 Andrews, E., Sheridan, P. J., and Ogren, J. A.: Seasonal differences in the vertical profiles of aerosol
 492 optical properties over rural Oklahoma, *Atmos. Chem. Phys.*, 11, 10661-10676, 10.5194/acp-11-10661-
 493 2011, 2011.
- 494 Andrews, E., Ogren, J. A., Kinne, S., and Samset, B.: Comparison of AOD, AAOD and column single
 495 scattering albedo from AERONET retrievals and in situ profiling measurements, *Atmos. Chem. Phys.*, 17,
 496 6041-6072, 10.5194/acp-17-6041-2017, 2017.
- 497 Arnott, W. P., Hamasha, K., Moosmüller, H., Sheridan, P. J., and Ogren, J. A.: Towards Aerosol Light-
 498 Absorption Measurements with a 7-Wavelength Aethalometer: Evaluation with a Photoacoustic
 499 Instrument and 3-Wavelength Nephelometer, *Aerosol Sci. Technol.*, 39, 17-29,
 500 10.1080/027868290901972, 2005.
- 501 Ban-Weiss, G. A., Cao, L., Bala, G., and Caldeira, K.: Dependence of climate forcing and response on
 502 the altitude of black carbon aerosols, *Clim. Dynam.*, 38, 897-911, 10.1007/s00382-011-1052-y, 2011.
- 503 Bergin, M. H., Cass, G. R., Xu, J., Fang, C., Zeng, L. M., Yu, T., Salmon, L. G., Kiang, C. S., Tang, X.
 504 Y., Zhang, Y. H., and Chameides, W. L.: Aerosol radiative, physical, and chemical properties in Beijing
 505 during June 1999, *J. Geophys. Res.*, 106, 17969-17980, Doi 10.1029/2001jd900073, 2001.
- 506 Bond, T. C., Doherty, S. J., Fahey, D. W., Forster, P. M., Berntsen, T., DeAngelo, B. J., Flanner, M. G.,
 507 Ghan, S., Kärcher, B., Koch, D., Kinne, S., Kondo, Y., Quinn, P. K., Sarofim, M. C., Schultz, M. G.,
 508 Schulz, M., Venkataraman, C., Zhang, H., Zhang, S., Bellouin, N., Guttikunda, S. K., Hopke, P. K.,
 509 Jacobson, M. Z., Kaiser, J. W., Klimont, Z., Lohmann, U., Schwarz, J. P., Shindell, D., Storelvmo, T.,
 510 Warren, S. G., and Zender, C. S.: Bounding the role of black carbon in the climate system: A scientific
 511 assessment, *J. Geophys. Res. Atmos.*, 118, 5380-5552, 10.1002/jgrd.50171, 2013.
- 512 Carrico, C. M., Rood, M. J., and Ogren, J. A.: Aerosol light scattering properties at Cape Grim, Tasmania,

513 during the First Aerosol Characterization Experiment (ACE 1), *J. Geophys. Res.*, 103, 16565,
 514 10.1029/98jd00685, 1998.

515 Cazorla, A., Bahadur, R., Suski, K. J., Cahill, J. F., Chand, D., Schmid, B., Ramanathan, V., and Prather,
 516 K. A.: Relating aerosol absorption due to soot, organic carbon, and dust to emission sources determined
 517 from in-situ chemical measurements, *Atmos. Chem. Phys.*, 13, 9337-9350, 10.5194/acp-13-9337-2013,
 518 2013.

519 Chakrabarty, R. K., Garro, M. A., Wilcox, E. M., and Moosmüller, H.: Strong radiative heating due to
 520 wintertime black carbon aerosols in the Brahmaputra River Valley, *Geophys. Res. Lett.*, 39, n/a-n/a,
 521 10.1029/2012gl051148, 2012.

522 Che, H., Zhang, X., Chen, H., Damiri, B., Goloub, P., Li, Z., Zhang, X., Wei, Y., Zhou, H., Dong, F., Li,
 523 D., and Zhou, T.: Instrument calibration and aerosol optical depth validation of the China Aerosol Remote
 524 Sensing Network, *J. Geophys. Res.*, 114, 10.1029/2008jd011030, 2009.

525 Chen, Y., Zhao, C., Zhang, Q., Deng, Z., Huang, M., and Ma, X.: Aircraft study of Mountain Chimney
 526 Effect of Beijing, China, *J. Geophys. Res.*, 114, 10.1029/2008jd010610, 2009.

527 Chung, C. E., Ramanathan, V., and Decremier, D.: Observationally constrained estimates of carbonaceous
 528 aerosol radiative forcing, *PNAS*, 109, 5, 10.1073/pnas.1203707109/-/DCSupplemental, 2012.

529 Ding, A. J., Huang, X., Nie, W., Sun, J. N., Kerminen, V. M., Petäjä, T., Su, H., Cheng, Y. F., Yang, X. Q.,
 530 Wang, M. H., Chi, X. G., Wang, J. P., Virkkula, A., Guo, W. D., Yuan, J., Wang, S. Y., Zhang, R. J., Wu,
 531 Y. F., Song, Y., Zhu, T., Zilitinkevich, S., Kulmala, M., and Fu, C. B.: Enhanced haze pollution by black
 532 carbon in megacities in China, *Geophys. Res. Lett.*, 43, 2873-2879, 10.1002/2016gl067745, 2016.

533 Drinovec, L., Gregorič, A., Zotter, P., Wolf, R., Bruns, E. A., Prévôt, A. S. H., Petit, J.-E., Favez, O.,
 534 Sciare, J., Arnold, I. J., Chakrabarty, R. K., Moosmüller, H., Filep, A., and Močnik, G.: The filter-loading
 535 effect by ambient aerosols in filter absorption photometers depends on the coating of the sampled particles,
 536 *Atmos. Meas. Tech.*, 10, 1043-1059, 10.5194/amt-10-1043-2017, 2017.

537 Ebert, M., Weinbruch, S., Rausch, A., Gorzawski, G., Helas, G., Hoffmann, P., and Wex, H.: Complex
 538 refractive index of aerosols during LACE 98 as derived from the analysis of individual particles, *J.*
 539 *Geophys. Res. Atmos.*, 107, LAC 3-1-LAC 3-15, 10.1029/2000jd000195, 2002.

540 Emde, C., Buras-Schnell, R., Kylling, A., Mayer, B., Gasteiger, J., Hamann, U., Kylling, J., Richter, B.,

541 Pause, C., Dowling, T., and Bugliaro, L.: The libRadtran software package for radiative transfer
 542 calculations (version 2.0.1), *Geosci. Model Dev.*, 9, 1647-1672, 10.5194/gmd-9-1647-2016, 2016.

543 Ervens, B., Turpin, B. J., and Weber, R. J.: Secondary organic aerosol formation in cloud droplets and
 544 aqueous particles (aqSOA): a review of laboratory, field and model studies, *Atmos. Chem. Phys.*, 11,
 545 11069-11102, 10.5194/acp-11-11069-2011, 2011.

546 Feng, Y., Ramanathan, V., and Kotamarthi, V. R.: Brown carbon: a significant atmospheric absorber of
 547 solar radiation?, *Atmos. Chem. Phys.*, 13, 8607-8621, 10.5194/acp-13-8607-2013, 2013.

548 Ferrero, L., Castelli, M., Ferrini, B. S., Moscatelli, M., Perrone, M. G., Sangiorgi, G., amp, apos, Angelo,
 549 L., Rovelli, G., Moroni, B., Scardazza, F., Močnik, G., Bolzacchini, E., Petitta, M., and Cappelletti, D.:
 550 Impact of black carbon aerosol over Italian basin valleys: high-resolution measurements along vertical
 551 profiles, radiative forcing and heating rate, *Atmos. Chem. Phys.*, 14, 9641-9664, 10.5194/acp-14-9641-
 552 2014, 2014.

553 Ferrero, L., Mocnik, G., Cogliati, S., Gregoric, A., Colombo, R., and Bolzacchini, E.: Heating Rate of
 554 Light Absorbing Aerosols: Time-Resolved Measurements, the Role of Clouds, and Source Identification,
 555 *Environ Sci Technol*, 52, 3546-3555, 10.1021/acs.est.7b04320, 2018.

556 Gao, R. S., Hall, S. R., Swartz, W. H., Schwarz, J. P., Spackman, J. R., Watts, L. A., Fahey, D. W., Aikin,
 557 K. C., Shetter, R. E., and Bui, T. P.: Calculations of solar shortwave heating rates due to black carbon and
 558 ozone absorption using in situ measurements, *J. Geophys. Res.*, 113, 10.1029/2007jd009358, 2008.

559 Gyawali, M., Arnott, W. P., and Moosmuller, H.: In situ aerosol optics in Reno, NV, USA, during and
 560 after the summer 2008 California wildfires and the influence of absorbing and non-absorbing organic
 561 coatings on spectral light absorption, *Atmos. Chem. Phys.*, 9, 8009-8015, 2009.

562 Hansen, A. D. A.: The Aethalometer Manual, Berkeley, California, USA, pp., 2005.

563 Haywood, J. M., Schwarzkopf, M. D., and Ramaswamy, V.: Estimates of radiative forcing due to modeled
 564 increases in tropospheric ozone, *J. Geophys. Res. Atmos.*, 103, 16999-17007, 10.1029/98jd01348, 1998.

565 He, X., Li, C. C., Lau, A. K. H., Deng, Z. Z., Mao, J. T., Wang, M. H., and Liu, X. Y.: An intensive study
 566 of aerosol optical properties in Beijing urban area, *Atmos. Chem. Phys.*, 9, 8903-8915, 2009.

567 Hodnebrog, O., Myhre, G., and Samset, B. H.: How shorter black carbon lifetime alters its climate effect,
 568 *Nat. Commun.*, 5, 1-7, 10.1038/ncomms6065, 2014.

569 Jing, J. S., Zhang, R. J., Tao, J., and Zhang, L. M.: Observations of Aerosol Optical Properties in the
570 Beijing Urban Area in Summer, *Atmos. Sci. Lett.*, 4, 338-343, 2011.

571 Kedia, S., Ramachandran, S., Kumar, A., and Sarin, M. M.: Spatiotemporal gradients in aerosol radiative
572 forcing and heating rate over Bay of Bengal and Arabian Sea derived on the basis of optical, physical,
573 and chemical properties, *J. Geophys. Res.*, 115, 10.1029/2009jd013136, 2010.

574 Kirchstetter, T. W., Novakov, T., and Hobbs, P. V.: Evidence that the spectral dependence of light
575 absorption by aerosols is affected by organic carbon, *J. Geophys. Res. Atmos.*, 109, n/a-n/a,
576 10.1029/2004jd004999, 2004.

577 Klingmüller, K., Lelieveld, J., Karydis, V. A., and Stenchikov, G. L.: Direct radiative effect of dust–
578 pollution interactions, *Atmos. Chem. Phys.*, 19, 7397-7408, 10.5194/acp-19-7397-2019, 2019.

579 Koch, D., and Del Genio, A. D.: Black carbon semi-direct effects on cloud cover: review and synthesis,
580 *Atmos. Chem. Phys.*, 10, 7685-7696, 10.5194/acp-10-7685-2010, 2010.

581 Lack, D. A., and Cappa, C. D.: Impact of brown and clear carbon on light absorption enhancement, single
582 scatter albedo and absorption wavelength dependence of black carbon, *Atmos. Chem. Phys.*, 10, 4207-
583 4220, 10.5194/acp-10-4207-2010, 2010.

584 Lack, D. A., Bahreni, R., Langridge, J. M., Gilman, J. B., and Middlebrook, A. M.: Brown carbon
585 absorption linked to organic mass tracers in biomass burning particles, *Atmos. Chem. Phys.*, 13, 2415-
586 2422, 10.5194/acp-13-2415-2013, 2013.

587 Laskin, A., Laskin, J., and Nizkorodov, S. A.: Chemistry of atmospheric brown carbon, *Chemical reviews*,
588 115, 4335-4382, 10.1021/cr5006167, 2015.

589 Lee, H. J., Aiona, P. K., Laskin, A., Laskin, J., and Nizkorodov, S. A.: Effect of solar radiation on the
590 optical properties and molecular composition of laboratory proxies of atmospheric brown carbon, *Environ.*
591 *Sci. Technol.*, 48, 10217-10226, 10.1021/es502515r, 2014.

592 Li, Z., Guo, J., Ding, A., Liao, H., Liu, J., Sun, Y., Wang, T., Xue, H., Zhang, H., and Zhu, B.: Aerosol
593 and boundary-layer interactions and impact on air quality, *National Science Review*, 4, 810-833,
594 10.1093/nsr/nwx117, 2017.

595 Liao, H., and Seinfeld, J. H.: Radiative forcing by mineral dust aerosols: Sensitivity to key variables, *J.*
596 *Geophys. Res. Atmos.*, 103, 31637-31645, 10.1029/1998jd200036, 1998.

597 Liu, D., Taylor, J. W., Young, D. E., Flynn, M. J., Coe, H., and Allan, J. D.: The effect of complex black
 598 carbon microphysics on the determination of the optical properties of brown carbon, *Geophys. Res. Lett.*,
 599 42, 613-619, 10.1002/2014gl062443, 2015a.

600 Liu, J., Scheuer, E., Dibb, J., Diskin, G. S., Ziemba, L. D., Thornhill, K. L., Anderson, B. E., Wisthaler,
 601 A., Mikoviny, T., Devi, J. J., Bergin, M., Perring, A. E., Markovic, M. Z., Schwarz, J. P., Campuzano-Jost,
 602 P., Day, D. A., Jimenez, J. L., and Weber, R. J.: Brown carbon aerosol in the North American continental
 603 troposphere: sources, abundance, and radiative forcing, *Atmos. Chem. Phys.*, 15, 7841-7858,
 604 10.5194/acp-15-7841-2015, 2015b.

605 Liu, P., Zhao, C., Liu, P., Deng, Z., Huang, M., Ma, X., and Tie, X.: Aircraft study of aerosol vertical
 606 distributions over Beijing and their optical properties, *Tellus B: Chemical and Physical Meteorology*, 61,
 607 756-767, 10.1111/j.1600-0889.2009.00440.x, 2009.

608 Müller, D., Lee, K. H., Gasteiger, J., Tesche, M., Weinzierl, B., Kandler, K., Müller, T., Toledano, C., Otto,
 609 S., Althausen, D., and Ansmann, A.: Comparison of optical and microphysical properties of pure Saharan
 610 mineral dust observed with AERONET Sun photometer, Raman lidar, and in situ instruments during
 611 SAMUM 2006, *J. Geophys. Res. Atmos.*, 117, n/a-n/a, 10.1029/2011jd016825, 2012.

612 Müller, T., Nowak, A., Wiedensohler, A., Sheridan, P., Laborde, M., Covert, D. S., Marinoni, A., Imre, K.,
 613 Henzing, B., Roger, J.-C., dos Santos, S. M., Wilhelm, R., Wang, Y.-Q., and de Leeuw, G.: Angular
 614 Illumination and Truncation of Three Different Integrating Nephelometers: Implications for Empirical,
 615 Size-Based Corrections, *Aerosol Sci. Technol.*, 43, 581-586, 10.1080/02786820902798484, 2009.

616 Mallet, M., Pont, V., Lioussé, C., Gomes, L., Pelon, J., Osborne, S., Haywood, J., Roger, J. C., Dubuisson,
 617 P., Mariscal, A., Thouret, V., and Goloub, P.: Aerosol direct radiative forcing over Djougou (northern
 618 Benin) during the African Monsoon Multidisciplinary Analysis dry season experiment (Special
 619 Observation Period-0), *J. Geophys. Res.*, 113, 10.1029/2007jd009419, 2008.

620 Massabò, D., Caponi, L., Bernardoni, V., Bove, M. C., Brotto, P., Calzolari, G., Cassola, F., Chiari, M.,
 621 Fedi, M. E., Fermo, P., Giannoni, M., Lucarelli, F., Nava, S., Piazzalunga, A., Valli, G., Vecchi, R., and
 622 Prati, P.: Multi-wavelength optical determination of black and brown carbon in atmospheric aerosols,
 623 *Atmos. Environ.*, 108, 1-12, 10.1016/j.atmosenv.2015.02.058, 2015.

624 Nakayama, T., Sato, K., Matsumi, Y., Imamura, T., Yamazaki, A., and Uchiyama, A.: Wavelength and

625 NO_x dependent complex refractive index of SOAs generated from the photooxidation of toluene, *Atmos.*
626 *Chem. Phys.*, 13, 531-545, 10.5194/acp-13-531-2013, 2013.

627 Nazarenko, L., Rind, D., Tsigaridis, K., Del Genio, A. D., Kelley, M., and Tausnev, N.: Interactive nature
628 of climate change and aerosol forcing, *J. Geophys. Res. Atmos.*, 122, 3457-3480, 10.1002/2016jd025809,
629 2017.

630 Nguyen, T. B., Lee, P. B., Updyke, K. M., Bones, D. L., Laskin, J., Laskin, A., and Nizkorodov, S. A.:
631 Formation of nitrogen- and sulfur-containing light-absorbing compounds accelerated by evaporation of
632 water from secondary organic aerosols, *J. Geophys. Res. Atmos.*, 117, n/a-n/a, 10.1029/2011jd016944,
633 2012.

634 Petaja, T., Jarvi, L., Kerminen, V. M., Ding, A. J., Sun, J. N., Nie, W., Kujansuu, J., Virkkula, A., Yang,
635 X. Q., Fu, C. B., Zilitinkevich, S., and Kulmala, M.: Enhanced air pollution via aerosol-boundary layer
636 feedback in China, *Sci. Repts.*, 6, 18998, 10.1038/srep18998, 2016.

637 Petra Seibert, F. B., Sven-Erik Gryning, Sylvain Joffre, Alix Rasmussen, Philippe Tercier: Review and
638 intercomparison of operational methods for the determination of the mixing height, *Atmos. Environ.*, 34,
639 27, 2000.

640 Quinn, P. K.: Aerosol optical properties during INDOEX 1999: Means, variability, and controlling factors,
641 *J. Geophys. Res.*, 107, 10.1029/2000jd000037, 2002.

642 Ramachandran, S., and Kedia, S.: Black carbon aerosols over an urban region: Radiative forcing and
643 climate impact, *J. Geophys. Res.*, 115, 10.1029/2009jd013560, 2010.

644 Ramana, M. V., Ramanathan, V., Kim, D., Roberts, G. C., and Corrigan, C. E.: Albedo, atmospheric solar
645 absorption and heating rate measurements with stacked UAVs, *Quarterly Journal of the Royal*
646 *Meteorological Society*, 133, 1913-1931, 10.1002/qj.172, 2007.

647 Ramana, M. V., Ramanathan, V., Feng, Y., Yoon, S. C., Kim, S. W., Carmichael, G. R., and Schauer, J. J.:
648 Warming influenced by the ratio of black carbon to sulphate and the black-carbon source, *Nature*
649 *Geoscience*, 3, 542-545, 10.1038/ngeo918, 2010.

650 Ramanathan, V., Crutzen, P. J., Kiehl, J. T., and Rosenfeld, D.: Aerosols, climate, and the hydrological
651 cycle, *Science*, 294, 2119-2124, 10.1126/science.1064034, 2001.

652 Ran, L., Deng, Z., Xu, X., Yan, P., Lin, W., Wang, Y., Tian, P., Wang, P., Pan, W., and Lu, D.: Vertical

653 profiles of black carbon measured by a micro-aethalometer in summer in the North China Plain, *Atmos.*
654 *Chem. Phys.*, 16, 10441-10454, 10.5194/acp-16-10441-2016, 2016a.

655 Ran, L., Deng, Z. Z., Wang, P. C., and Xia, X. A.: Black carbon and wavelength-dependent aerosol
656 absorption in the North China Plain based on two-year aethalometer measurements, *Atmos. Environ.*, 142,
657 132-144, 10.1016/j.atmosenv.2016.07.014, 2016b.

658 Rosati, B., Herrmann, E., Bucci, S., Fierli, F., Cairo, F., Gysel, M., Tillmann, R., Größ, J., Gobbi, G. P.,
659 Di Liberto, L., Di Donfrancesco, G., Wiedensohler, A., Weingartner, E., Virtanen, A., Mentel, T. F., and
660 Baltensperger, U.: Studying the vertical aerosol extinction coefficient by comparing in situ airborne data
661 and elastic backscatter lidar, *Atmos. Chem. Phys.*, 16, 4539-4554, 10.5194/acp-16-4539-2016, 2016.

662 Sührling, M., Maronga, B., Herbolt, F., and Raasch, S.: On the Effect of Surface Heat-Flux Heterogeneities
663 on the Mixed-Layer-Top Entrainment, *Boundary-Layer Meteorol.*, 151, 531-556, 10.1007/s10546-014-
664 9913-7, 2014.

665 Sahu, L. K., Kondo, Y., Moteki, N., Takegawa, N., Zhao, Y., Cubison, M. J., Jimenez, J. L., Vay, S., Diskin,
666 G. S., Wisthaler, A., Mikoviny, T., Huey, L. G., Weinheimer, A. J., and Knapp, D. J.: Emission
667 characteristics of black carbon in anthropogenic and biomass burning plumes over California during
668 ARCTAS-CARB 2008, *J. Geophys. Res. Atmos.*, 117, n/a-n/a, 10.1029/2011jd017401, 2012.

669 Saleh, R., Marks, M., Heo, J., Adams, P. J., Donahue, N. M., and Robinson, A. L.: Contribution of brown
670 carbon and lensing to the direct radiative effect of carbonaceous aerosols from biomass and biofuel
671 burning emissions, *J. Geophys. Res.*, 120, 10285-10296, 10.1002/, 2015.

672 Sareen, N., Moussa, S. G., and McNeill, V. F.: Photochemical aging of light-absorbing secondary organic
673 aerosol material, *The journal of physical chemistry. A*, 117, 2987-2996, 10.1021/jp309413j, 2013.

674 Schnaiter, M., Schmid, O., Petzold, A., Fritzsche, L., Klein, K. F., Andreae, M. O., Helas, G., Thielmann,
675 A., Gimmler, M., Möhler, O., Linke, C., and Schurath, U.: Measurement of Wavelength-Resolved Light
676 Absorption by Aerosols Utilizing a UV-VIS Extinction Cell, *Aerosol Sci. Technol.*, 39, 249-260,
677 10.1080/027868290925958, 2005.

678 Shamjad, P. M., Tripathi, S. N., Pathak, R., Hallquist, M., Arola, A., and Bergin, M. H.: Contribution of
679 Brown Carbon to Direct Radiative Forcing over the Indo-Gangetic Plain, *Environ Sci Technol*, 49, 10474-
680 10481, 10.1021/acs.est.5b03368, 2015.

681 Su, T., Li, J., Li, C., Xiang, P., Lau, A. K.-H., Guo, J., Yang, D., and Miao, Y.: An intercomparison of
 682 long-term planetary boundary layer heights retrieved from CALIPSO, ground-based lidar, and radiosonde
 683 measurements over Hong Kong, *J. Geophys. Res. Atmos.*, 122, 3929-3943, 10.1002/2016jd025937, 2017.
 684 Sun, J., Zhi, G., Hitzenberger, R., Chen, Y., Tian, C., Zhang, Y., Feng, Y., Cheng, M., Zhang, Y., Cai, J.,
 685 Chen, F., Qiu, Y., Jiang, Z., Li, J., Zhang, G., and Mo, Y.: Emission factors and light absorption properties
 686 of brown carbon from household coal combustion in China, *Atmos. Chem. Phys.*, 17, 4769-4780,
 687 10.5194/acp-17-4769-2017, 2017.
 688 Tian, P., Liu, D., Huang, M., Liu, Q., Zhao, D., Ran, L., Deng, Z., Wu, Y., Fu, S., Bi, K., Gao, Q., He, H.,
 689 Xue, H., and Ding, D.: The evolution of an aerosol event observed from aircraft in Beijing: An insight
 690 into regional pollution transport, *Atmos. Environ.*, 206, 11-20, 10.1016/j.atmosenv.2019.02.005, 2019.
 691 Torres, B., Dubovik, O., Toledano, C., Berjon, A., Cachorro, V. E., Lapyonok, T., Litvinov, P., and Goloub,
 692 P.: Sensitivity of aerosol retrieval to geometrical configuration of ground-based sun/sky radiometer
 693 observations, *Atmos. Chem. Phys.*, 14, 847-875, 10.5194/acp-14-847-2014, 2014.
 694 Tripathi, S. N., Srivastava, A. K., Dey, S., Satheesh, S. K., and Krishnamoorthy, K.: The vertical profile
 695 of atmospheric heating rate of black carbon aerosols at Kanpur in northern India, *Atmos. Environ.*, 41,
 696 6909-6915, 10.1016/j.atmosenv.2007.06.032, 2007.
 697 Updyke, K. M., Nguyen, T. B., and Nizkorodov, S. A.: Formation of brown carbon via reactions of
 698 ammonia with secondary organic aerosols from biogenic and anthropogenic precursors, *Atmos. Environ.*,
 699 63, 22-31, 10.1016/j.atmosenv.2012.09.012, 2012.
 700 Wang, F., Li, Z., Ren, X., Jiang, Q., He, H., Dickerson, R. R., Dong, X., and Lv, F.: Vertical distributions
 701 of aerosol optical properties during the spring 2016 ARIAs airborne campaign in the North China Plain,
 702 *Atmos. Chem. Phys.*, 18, 8995-9010, 10.5194/acp-18-8995-2018, 2018a.
 703 Wang, J., Nie, W., Cheng, Y., Shen, Y., Chi, X., Wang, J., Huang, X., Xie, Y., Sun, P., Xu, Z., Qi, X., Su,
 704 H., and Ding, A.: Light absorption of brown carbon in eastern China based on 3-year multi-wavelength
 705 aerosol optical property observations and an improved absorption Ångström exponent segregation
 706 method, *Atmos. Chem. Phys.*, 18, 9061-9074, 10.5194/acp-18-9061-2018, 2018b.
 707 Wang, Y., Che, H., Ma, J., Wang, Q., Shi, G., Chen, H., Goloub, P., and Hao, X.: Aerosol radiative forcing
 708 under clear, hazy, foggy, and dusty weather conditions over Beijing, China, *Geophys. Res. Lett.*, 36,

10.1029/2009gl037181, 2009.

Wang, Z., Huang, X., and Ding, A.: Dome effect of black carbon and its key influencing factors: a one-dimensional modelling study, *Atmos. Chem. Phys.*, 18, 2821-2834, 10.5194/acp-18-2821-2018, 2018c.

Wilcox, E. M., Thomas, R. M., Praveen, P. S., Pistone, K., Bender, F. A., and Ramanathan, V.: Black carbon solar absorption suppresses turbulence in the atmospheric boundary layer, *Proc. Natl. Acad. Sci. USA.*, 113, 11794-11799, 10.1073/pnas.1525746113, 2016.

Wong, J. P. S., Tsagkaraki, M., Tsiodra, I., Mihalopoulos, N., Violaki, K., Kanakidou, M., Sciare, J., Nenes, A., and Weber, R. J.: Atmospheric evolution of molecular-weight-separated brown carbon from biomass burning, *Atmos. Chem. Phys.*, 19, 7319-7334, 10.5194/acp-19-7319-2019, 2019.

Wu, Y., Wang, X., Tao, J., Huang, R., Tian, P., Cao, J., Zhang, L., Ho, K.-F., Han, Z., and Zhang, R.: Size distribution and source of black carbon aerosol in urban Beijing during winter haze episodes, *Atmos. Chem. Phys.*, 17, 7965-7975, 10.5194/acp-17-7965-2017, 2017.

Xia, X., Eck, T. F., Holben, B. N., Phillippe, G., and Chen, H.: Analysis of the weekly cycle of aerosol optical depth using AERONET and MODIS data, *J. Geophys. Res.*, 113, 10.1029/2007jd009604, 2008.

Xie, C., Xu, W., Wang, J., Wang, Q., Liu, D., Tang, G., Chen, P., Du, W., Zhao, J., Zhang, Y., Zhou, W., Han, T., Bian, Q., Li, J., Fu, P., Wang, Z., Ge, X., Allan, J., Coe, H., and Sun, Y.: Vertical characterization of aerosol optical properties and brown carbon in winter in urban Beijing, China, *Atmos. Chem. Phys.*, 19, 165-179, 10.5194/acp-19-165-2019, 2019.

Yu, H., Liu, S. C., and Dickinson, R. E.: Radiative effects of aerosols on the evolution of the atmospheric boundary layer, *J. Geophys. Res.*, 107, 10.1029/2001jd000754, 2002.

Yu, P. F., Toon, O. B., Bardeen, C. G., Zhu, Y. Q., Rosenlof, K. H., Portmann, R. W., Thornberry, T. D., Gao, R. S., SDavis, S. M., Wolf, E. T., Gouw, J. D., Peterson, D. A., Fromm, M. D., and Robock, A.: Black carbon lofts wildfire smoke high into the stratosphere to form a persistent plume, *Science*, 365, 14, 2019.

Zhang, R., Jing, J., Tao, J., Hsu, S. C., Wang, G., Cao, J., Lee, C. S. L., Zhu, L., Chen, Z., Zhao, Y., and Shen, Z.: Chemical characterization and source apportionment of PM_{2.5} in Beijing: seasonal perspective, *Atmos. Chem. Phys.*, 13, 7053-7074, 10.5194/acp-13-7053-2013, 2013.

Zhang, X. Y., Wang, J. Z., Wang, Y. Q., Liu, H. L., Sun, J. Y., and Zhang, Y. M.: Changes in chemical

737 components of aerosol particles in different haze regions in China from 2006 to 2013 and contribution of
738 meteorological factors, *Atmos. Chem. Phys.*, 15, 12935-12952, 10.5194/acp-15-12935-2015, 2015.

739 Zhang, Y., Forrister, H., Liu, J., Dibb, J., Anderson, B., Schwarz, J. P., Perring, A. E., Jimenez, J. L.,
740 Campuzano-Jost, P., Wang, Y., Nenes, A., and Weber, R. J.: Top-of-atmosphere radiative forcing affected
741 by brown carbon in the upper troposphere, *Nature Geoscience*, 10.1038/ngeo2960, 2017.

742 Zhao, D. L., Huang, M. Y., Tian, P., He, H., Lowe, D., Zhou, W., Sheng, J. J., Wang, F., Bi, K., Kong, S.
743 F., Yang, Y., Liu, Q., Liu, D. T., and Ding, D. P.: Vertical characteristics of black carbon physical properties
744 over Beijing region in warm and cold seasons, *Atmos. Environ.*, 213, 296-310, 2019a.

745 Zhao, G., Zhao, C. S., Kung, Y., Bian, Y. X., Tao, J. C., Shen, C. Y., and Yu, Y. L.: Calculating the aerosol
746 asymmetry factor based on measurements from the humidified nephelometer system, *Atmos. Chem. Phys.*,
747 18, 9049-9060, 10.5194/acp-18-9049-2018, 2018.

748 Zhao, P. S., Ding, J., Du, X., and Su, J.: High time-resolution measurement of light scattering hygroscopic
749 growth factor in Beijing A novel method for high relative humidity conditions, *Atmos. Environ.*, 215,
750 10.1016/j.atmosenv.2019.116912, 2019b.

751 Zhao, R., Lee, A. K. Y., Huang, L., Li, X., Yang, F., and Abbatt, J. P. D.: Photochemical processing of
752 aqueous atmospheric brown carbon, *Atmos. Chem. Phys.*, 15, 6087-6100, 10.5194/acp-15-6087-2015,
753 2015.

754 Zhong, J., Zhang, X., Dong, Y., Wang, Y., Liu, C., Wang, J., Zhang, Y., and Che, H.: Feedback effects of
755 boundary-layer meteorological factors on cumulative explosive growth of $PM_{2.5}$
756 during winter heavy pollution episodes in Beijing from 2013 to 2016, *Atmos. Chem. Phys.*, 18, 247-258,
757 10.5194/acp-18-247-2018, 2018.

758
759

760

Table 1. Flight summary in this study.

Flight number	Time range Local time	Case	Pollution period	Mixing layer height
RF1	20161115 12:00	Case_1	CP	1450 m
RF2	20161115 14:00	Case_1	CP	1450 m
RF3	20161116 12:00	Case_1	TP	850 m
RF4	20161116 14:00	Case_1	TP	750 m
RF5	20161117 12:00	Case_1	TP(Cloud)	1250 m
RF6	20161117 14:00	Case_1	TP(Cloud)	1150 m
RF7	20161118 12:00	Case_1	HP(Cloud)	1050 m
RF8	20161210 14:00	Case_2	CP	950 m
RF9	20161211 14:00	Case_2	MP	950 m
RF10	20161212 14:00	Case_2	HP	450 m
RF11	20161216 14:00	Case_3	TP	350 m
RF12	20161217 14:00	Case_3	HP	350 m
RF13	20161218 14:00	Case_3	HP	350 m
RF14	20161219 14:00	Case_3	HP	250 m

761

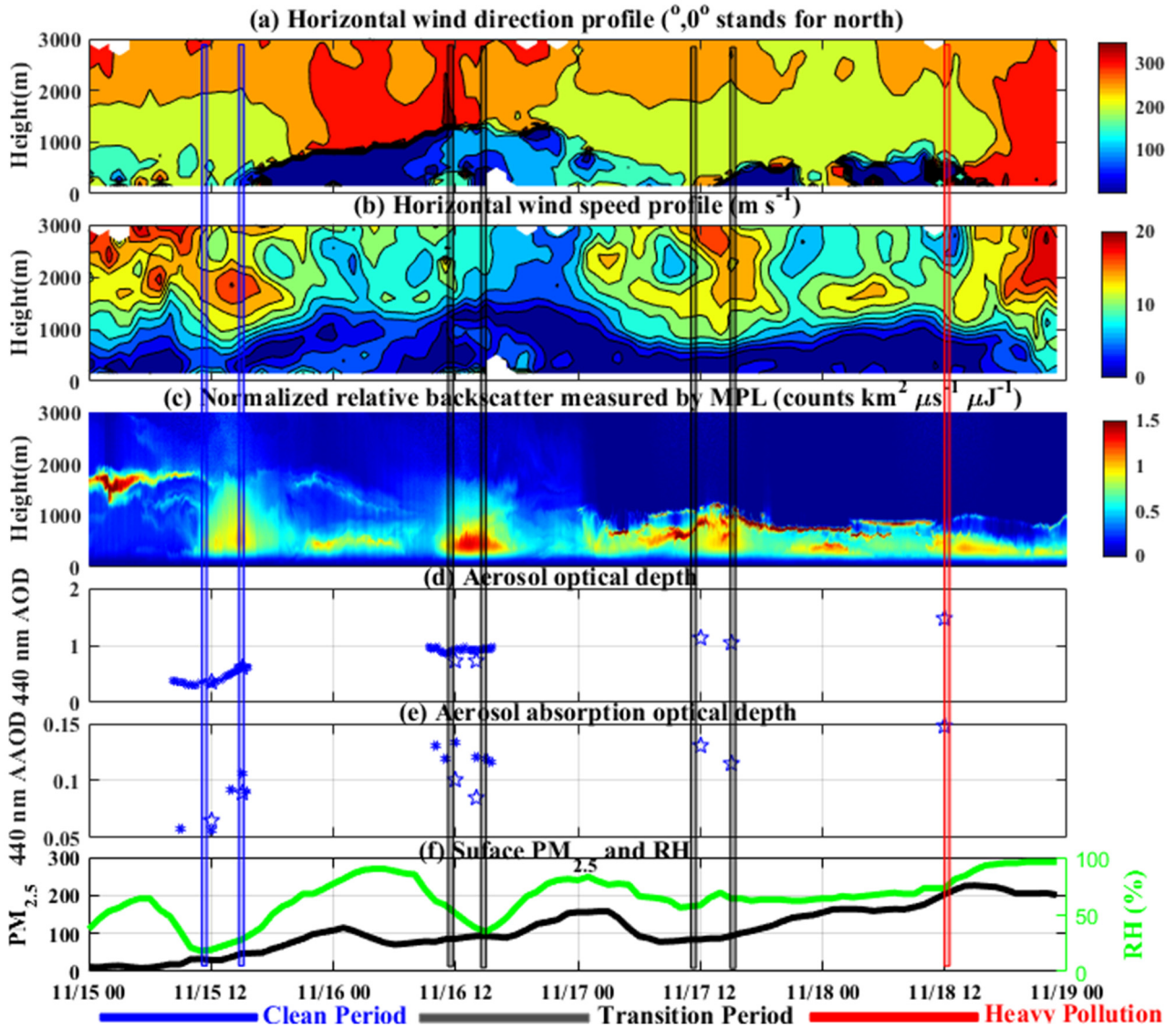
¹ CP, TP, and HP represents the clean, transition and high pollution period during a pollution event.

762

763 Table 2. Summary of input parameters for the radiative transfer calculation using Discrete Ordinates
764 Radiative Transfer Code (DISORT)
765

Parameter	Input value
Radiative transfer solver	DISORT, 12-streams, delta-m method
Gas absorption parameterization	LOWTRAN/SBDART parameterization
Wavelength range	250-2550nm
Atmosphere	Standard Mid-latitude atmosphere
Aerosol	The 25 layers from the surface to 5000 m was chosen inside the DISORT, and every 200 m average aerosol optical properties at 550 nm was used; AOD values are derived from in-situ Aurora3000 and AE33 measurements, also applying an exponential λ -dependent function SSA values are from in-situ σ_{sca} and σ_{abs} measurement SAE values are from in-situ Aurora3000 measurement AAE values are from in-situ AE33 measurement Asymmetry factor (g) is derived from the Aurora3000 measurement and uses Henyey-Greenstein phase function
Location	39.54°N, 116.23°E
Time	Flight time
Solar zenith angle	Effective solar zenith angle Using local time and aircraft location
Surface albedo	IGBP surface type 13 (Urban)

766
767



769

770

771

772

773

774

775

776

Fig. 1. Temporal variations from Nov. 15th to 18th of vertical profiles of wind direction (a), and wind speed (b) measured by wind profile radar; (c) particle extinction measured by MPL lidar; (d) aerosol optical depth (d) and aerosol absorption optical depth (e) from AERONET (asterisk) and derived from aircraft in-situ measurements (open star)(f) surface $\text{PM}_{2.5}$ and RH.). The vertical bars denote the periods of flight profiles, with blue, black and red representing the clean period, transition period and heavy pollution during a pollution event, respectively. The other two pollution events are shown in the

778

779

780

781

782

783

784

785

786

787

788

789

790

791

792

793

794

795

796

797

798

799

800

801

802

803

804

805

806

807

808

809

810

811

812

813

814

815

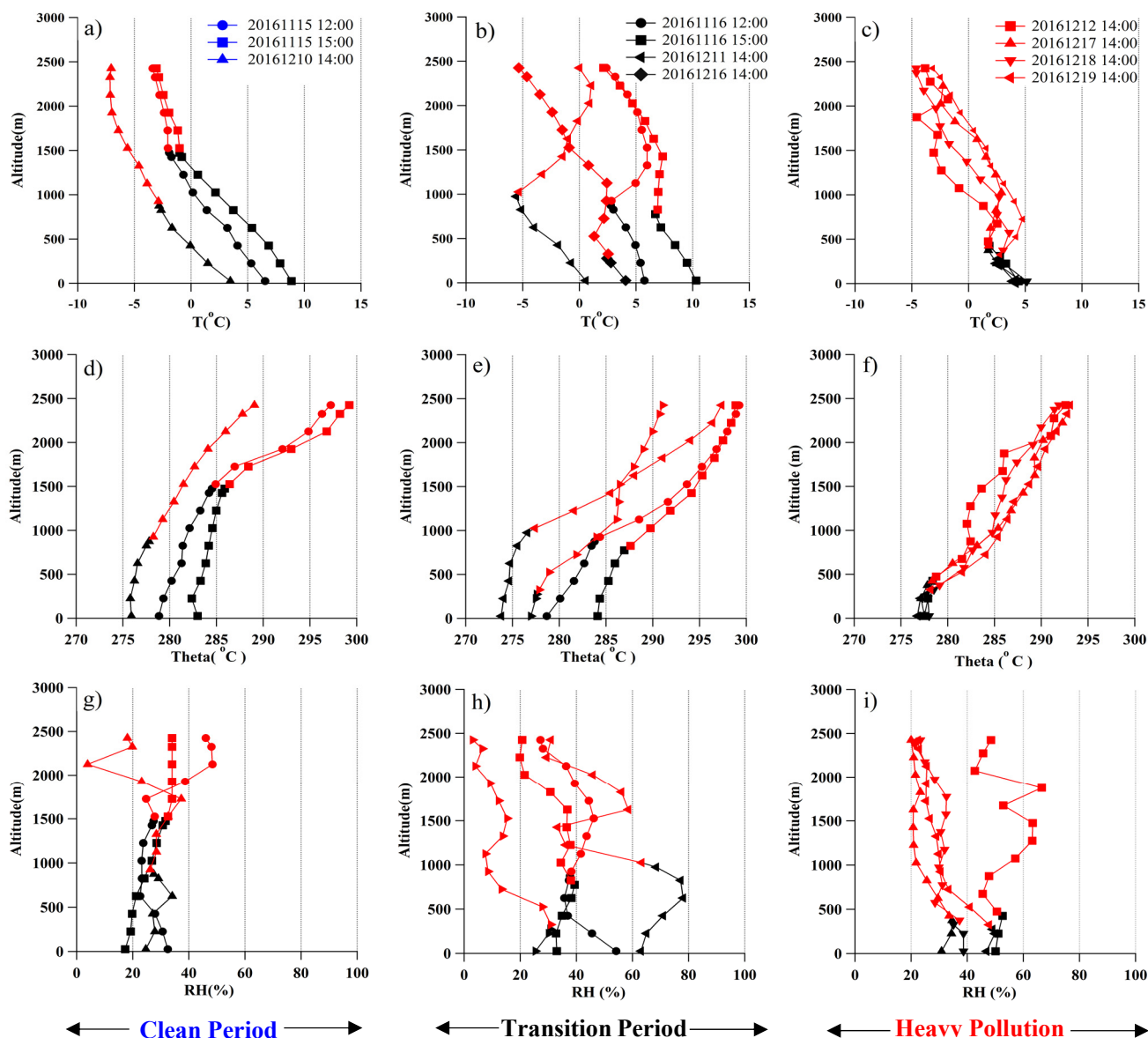
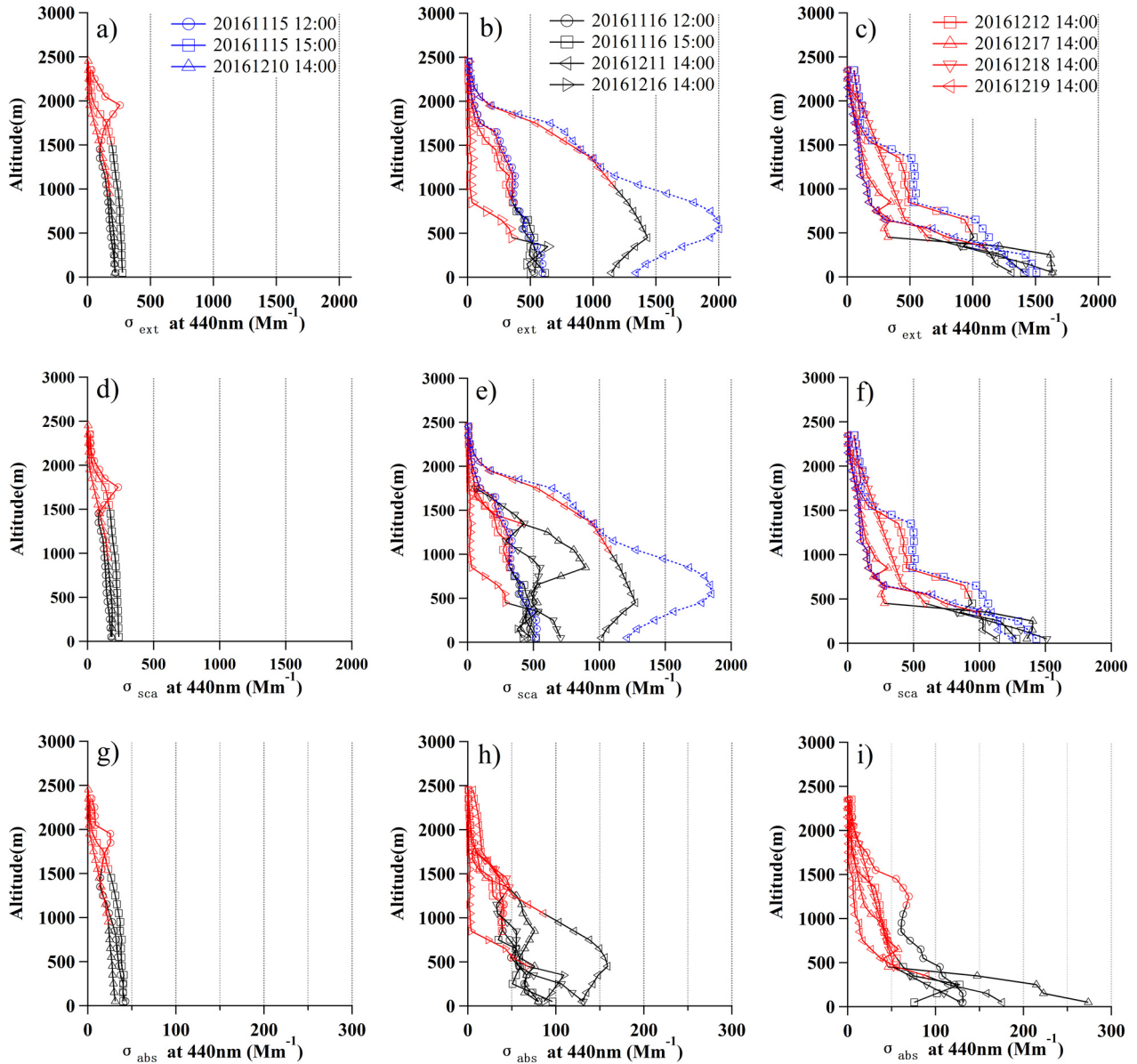


Fig. 2. Vertical profiles of temperature (a, b, c), relative humidity (d, e, f) and potential temperature (g, h, i) for Clean Period, Transition Period and Heavy Pollution period, respectively. The black and red dots represent for inside the PBL and above the PBL.



← **Clean Period** → ← **Transition Period** → ← **Pollution Period** →

Fig. 3. Vertical profiles of aerosol extinction, scattering and absorption coefficient at 440 nm for CP (blue), TP (black) and HP period (red), respectively. The black and red lines represent for inside and above the ML, respectively. The hygroscopic-corrected profiles are shown as blue lines.

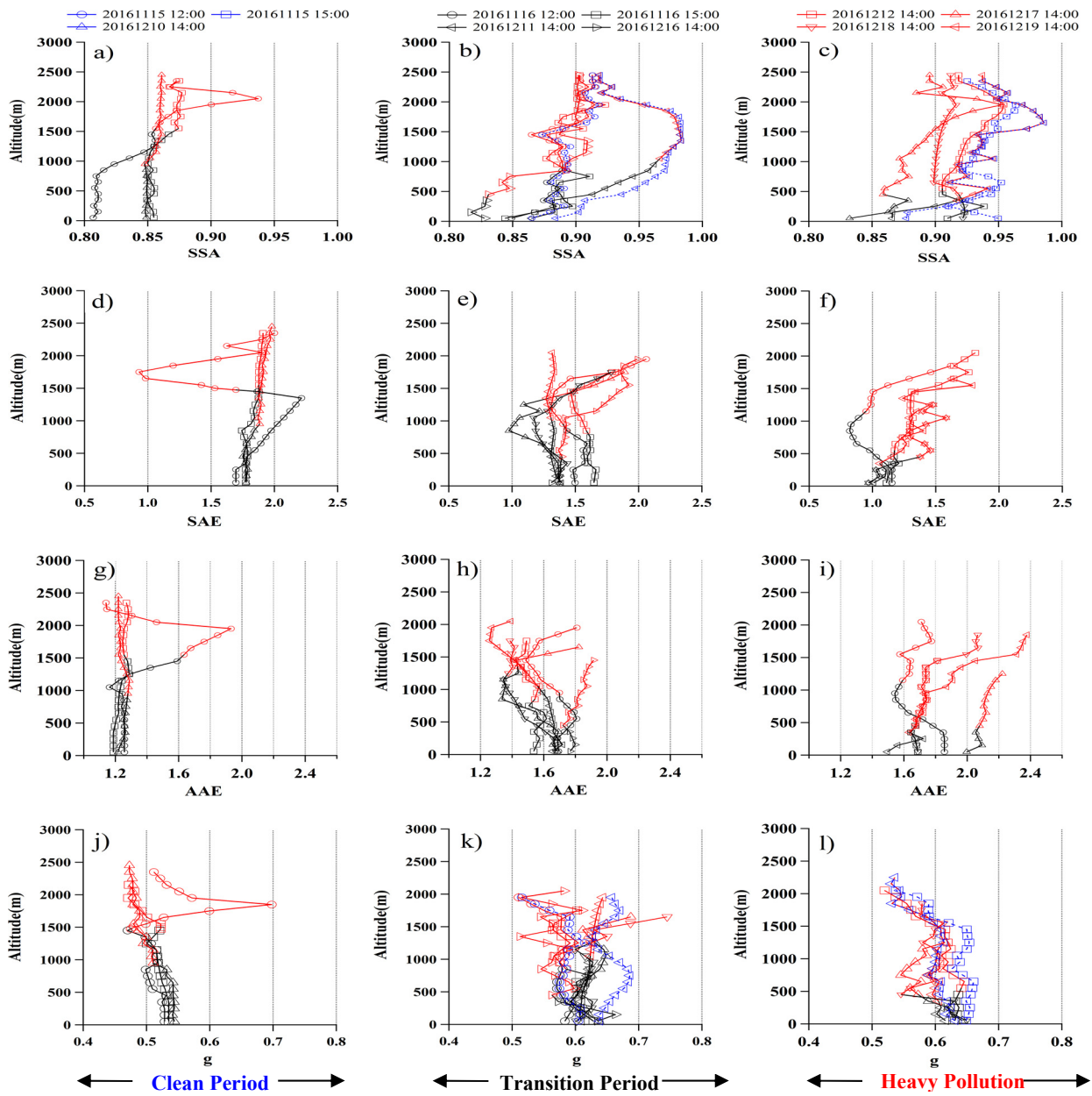


Fig. 4. Vertical profiles of aerosol single scattering albedo at 440 nm (SSA, a - c), scattering Angström exponent (SAE, d - f), absorption Angström exponent (AAE, g - i), and asymmetry parameter (g, j - l) for CP (left panel), TP (middle panel) and HP period (right panel), respectively. The hygroscopicity

corrected profiles was shown in blue lines.

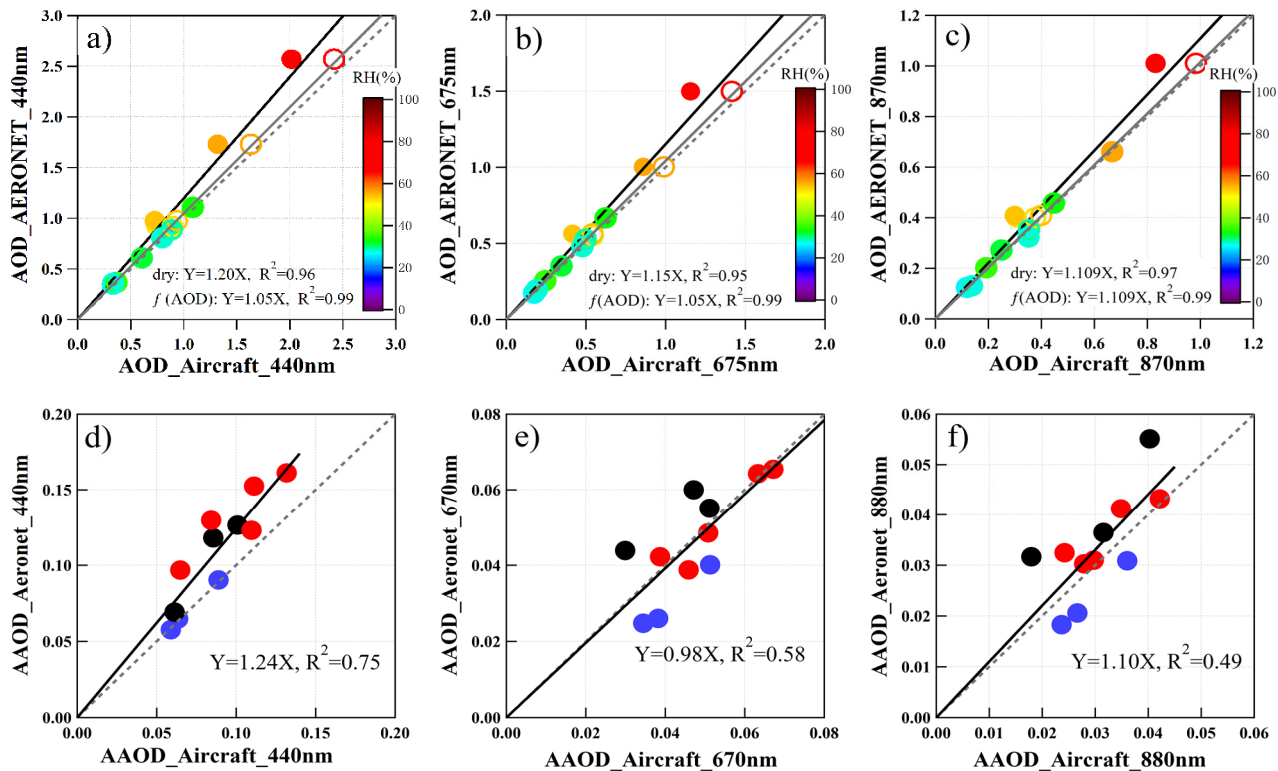
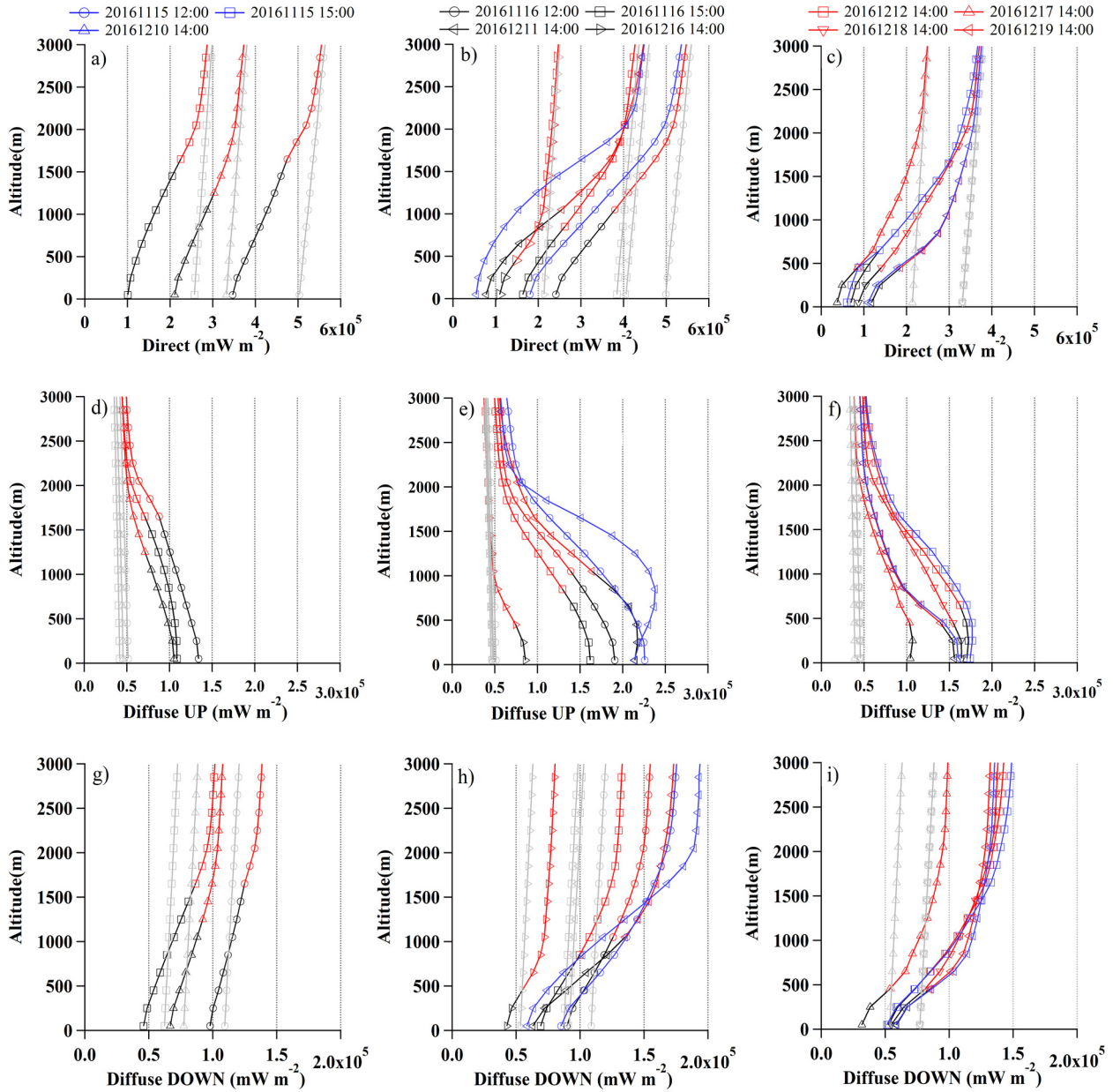


Fig. 5. Comparison between AERONET and aircraft in-situ constrained AOD and AAOD: a) - c) The comparison of AOD at 440nm, 675nm, and 870nm colored by RH; the solid and open markers denote the dry and hygroscopicity-corrected conditions; d) – f) Comparison of AAOD at 440nm, 670nm, and 880nm. The blue, black, and red circles represent the CP, TP, and HP periods, respectively.



← Clean Period →
← Transition Period →
← Pollution Period →

Fig. 6. Radiative transfer results calculated by DISTORT. a)-c), b)-e), and g)-i) show the direct, diffuse upward and diffuse downward irradiance respectively. The left, middle and right panel represent for CP, TP and HP period respectively, with black and red lines denoting above and within the PBL. The

colored and grey lines denote the profiles for with and without aerosol influence, respectively, and the blue lines are for corrected hygroscopic effect.

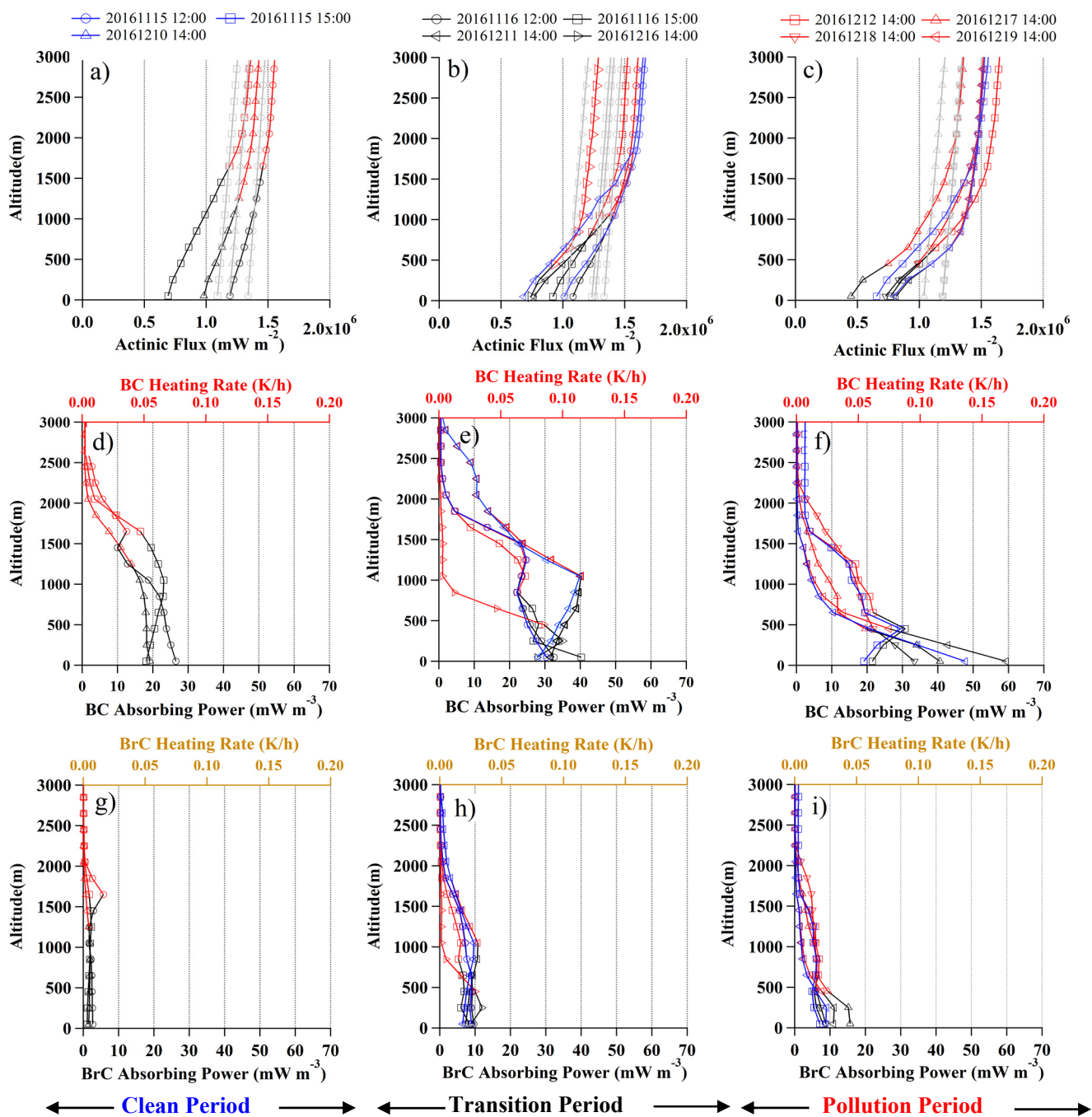


Fig. 7. Actinic flux (a-c), BC absorbing power (d-f) and BrC absorbing power (g-i). The left, middle and

right panel is for LP, TP and HP respectively, with the black and red line denoting within and above the PBL. The gray lines in a) to c) show the aerosol free results and the blue line denote the corrected hygroscopic effect. The upper x-axis from d) to i) shows the heating rate.

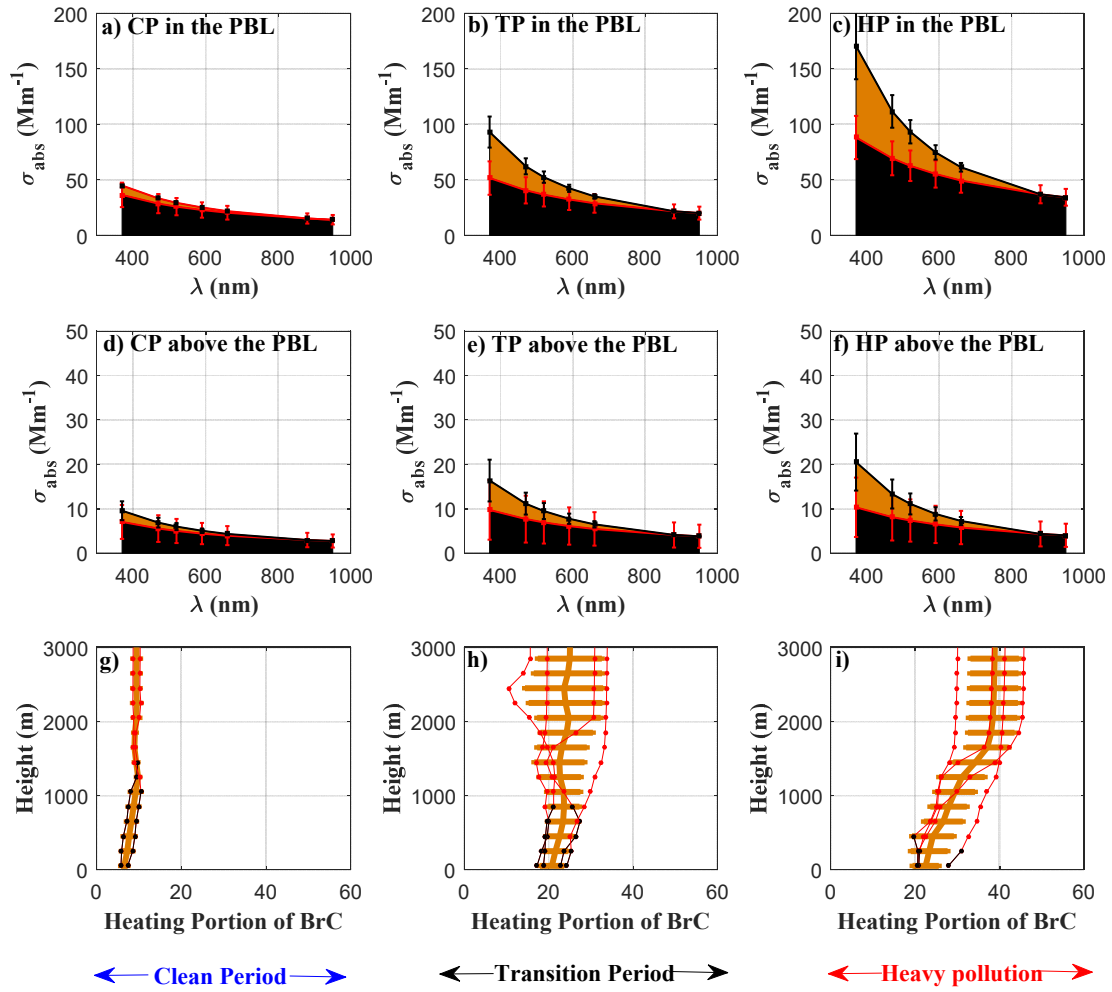


Fig. 8. Spectral absorption coefficient of BC and BrC inside and above the PBL for CP (a, d), TP (b, e) and HP period (c, f), respectively, shown in black and brown carbon color respectively. The vertical profiles of heating portion of BrC for CP, TP and HP period are shown in g) – i).